Sensitivity of Modeled Precipitation to Sea Surface Temperature in Regions with Complex Topography and Coastlines: A Case Study for the Mediterranean

ALFONSO SENATORE AND GIUSEPPE MENDICINO

Department of Environmental and Chemical Engineering, University of Calabria, Rende, Italy

HANS RICHARD KNOCHE AND HARALD KUNSTMANN

Institute of Meteorology and Climate Research–Atmospheric Environmental Research (IMK-IFU),
Karlsruhe Institute of Technology, Garmisch-Partenkirchen, Germany

(Manuscript received 18 May 2013, in final form 2 July 2014)

ABSTRACT

An analysis of the effects of SST representation on precipitation in long-term continuous simulations was carried out for the Mediterranean peninsula of Calabria, Italy, which is characterized by complex coastlines and orography. A parameterization analysis was performed to find an optimal model configuration, using a method where SST fields are directly ingested from NCEP datasets into the Weather Research and Forecasting (WRF) Model lower boundary condition files. The results of the optimal configuration were used for a comparison with recorded precipitation patterns for a very wet period (from November 2008 to January 2009), adopting several interpolation options available in the WRF Preprocessing System. An additional comparison was made against a uniform variation of the original SST fields by $\varepsilon = \pm 0.5$ K. It was found that the interpolation options mainly affect near-coastline SSTs, where methods requiring fewer source data points have several advantages. Effects of SST representation on precipitation, accumulated over the whole 3-month period, are generally lower than ±2%, but a specific class of events (synoptic situations) with strong differences in precipitation patterns was identified. These events are connected to pressure systems moving from the African coast to the north and approaching the Sicilian and Calabrian coastlines. Two of these events, which occurred on 27–29 December 2008 and 9 January 2009, were analyzed in detail, highlighting that small variations of SST values induce slight shifts in the paths of the weather fronts. These slight shifts are important enough to determine whether or not wet air masses can reach the mountain ranges close to the coast, where rainfall intensity is enhanced by orographic effects.

1. Introduction

Observations show that sea surface temperatures (SSTs) often play a major role in midlatitude extreme precipitation events (e.g., caused by atmospheric rivers; Neiman et al. 2013). This is especially true in areas such as the Mediterranean (Rebora et al. 2013), where sea–atmosphere interactions are influenced by complex coastal orography, leading to local meteorological processes whose complexity is often not fully interpreted by models (Senatore et al. 2011). The impact of SST representation in meteorological models like the Weather Research and Forecasting (WRF) Model (Skamarock et al. 2008) has been widely analyzed in recent years, since this physical variable directly affects the development of mesoscale meteorological processes in coastal areas up to several hundred kilometers inland. Many studies that use WRF for analyzing the strong relationship of SSTs with several extreme phenomena are available, such as those proposed by Bond et al. (2010) for tropical cyclones, Miglietta et al. (2011) for Mediterranean hurricanes, Sijikumar and Rajeev (2012) for the Indian summer monsoon, Jung et al. (2012) for heavy snowfall, and Booth et al. (2012) for midlatitude storms near the Gulf Stream. Some sensitivity experiments specifically focused on assessing orographic forcing by means of the reduction/exclusion of mountain barriers (Hong and Lee 2009; Smith et al. 2010; Flesch and Reuter 2012), while in some other studies both SSTs

---

Corresponding author address: Alfonso Senatore, Dept. of Environmental and Chemical Engineering, University of Calabria, via P. Bucci 41b, 87036 Rende (CS), Italy.
E-mail: alfonso.senatore@unical.it

DOI: 10.1175/JHM-D-13-089.1

and orography were varied (for the West African monsoon; Flaounas et al. 2012).

The effect of an improved space–time resolution of the SST boundary conditions was also assessed for several meteorological processes. Bongirwar et al. (2011) evaluated the impact of an improved satellite-based SST resolution on the simulation of tropical cyclones. Song et al. (2009) analyzed the influence of SST resolution on numerical simulations of air–sea coupling near oceanic fronts. LaCasse et al. (2008) assessed the WRF Model simulation sensitivity over oceanic regions around Florida to high-resolution SSTs, while Case et al. (2011) used the same data over the same area to improve simulations of summertime pulse-type convective precipitation. Chen et al. (2011) tested the effects of different SST space–time resolutions on stagnation in a large urbanized area. Cha et al. (2011) used high-resolution SST products and idealized SST distributions to simulate snowfall over the Yellow Sea.

Further studies investigated the effect of time constant or varying SST over periods of several days (e.g., Borge et al. 2008); others compared results from simulations using SST reanalysis with results provided by the coupled run of oceanic models [e.g., Lebeaupin Brossier and Drobinski (2009) and Boé et al. (2011), who considered the orographic effect on mesoscale variations in wind, and Ratnam et al. (2012), who put a particular emphasis on the sensitivity of precipitation fields]. A smaller number of studies focused on the influence of the quality of the SST data in reproducing coastal small-scale features (Muller et al. 2007). These are very difficult to simulate, especially when influenced by complex coastlines and very steep terrain (e.g., Papanastasiou et al. 2010).

This study aims to extend the available experiments to a specific problem, which becomes particularly important for precipitation simulations in regions characterized by complex coastlines: the representation of SST fields in WRF mesoscale models, once the desired data source is selected, by means of the most suitable interpolation and ingestion techniques. This is a nontrivial problem, which, if addressed improperly, can deteriorate the modeled precipitation output. For example, in Caldwell et al. (2009), direct interpolation of WRF SST from surface temperature provided by a climate system model corrupts near-coastal SST with land surface temperature values leading to an overprediction of surface moisture flux. Besides a wide choice of interpolation methods, further possibilities exist for improving the SST representation. For example, since WRF, version 3.1, the *sst skin* option is available to calculate skin SST based on Zeng and Beljaars (2005), who derive a prognostic scheme that reliably reproduces the SST diurnal cycle, which increases the temporal resolution (usually updated daily or weekly) of the SST variable.

Few applications are available in the literature showing the sensitivity of mesoscale models to SST field interpolation and ingestion methods. Recently, van Dijke and Vonk (2011) suggested an operational technique in WRF to address problems related to the initialization of the skin surface temperature of water points near the coast of The Netherlands using European Centre for Medium-Range Weather Forecasts (ECMWF) data. This method is based on the comparison of coastal grid points with the average SST of the surrounding sea grid points, where the latter are selected through a modified threshold for the ECMWF fractional land mask values. If the differences are too large, the actual values are replaced by average SST values through an iterative process.

Among possible alternatives, in this paper a method is used based on the external manipulation of SST products and their replacement in the WRF lower boundary conditions file. A modification of the threshold for land mask values or similar is not required in this approach. The improved SST fields are used in the preliminary search for the optimal model configuration in the northern part of Calabria, a southern Italian peninsula located in the middle of the Mediterranean basin characterized by long complex coastlines, which are often surrounded by steep mountains. Several parameterization analyses are available for Mediterranean regions with complex terrain (e.g., Givati et al. 2012), but to the best of our knowledge, so far only one study focused on northern Calabria (Schurmann et al. 2009). Based on the WRF Model coupled with chemistry (WRF-Chem), the authors analyzed the model capability in reproducing ozone concentrations, choosing four periods of 5–7 days. A larger number of WRF applications are reported for southeastern Italy (e.g., Miglietta and Regano 2008; Bertotti et al. 2009; Mastrangelo et al. 2011; Miglietta et al. 2011). For this region, a forecasting system was also developed for operational weather prediction (available at http://meteo.le.isac.cnr.it/METEO/wrf.php). So far, all studies on southern Italy focused on the analysis of extreme events lasting only a few days.

Once the best configuration for the analyzed region is determined, the main focus of this paper is to assess whether, and to what extent, different interpolation and ingestion techniques of SST data affect precipitation patterns in the analyzed domain, especially over land, during long-term continuous simulations. For this purpose, we compare model results for a very wet 3-month period that are obtained by using several interpolation procedures available in WRF, as well as by sensitivity

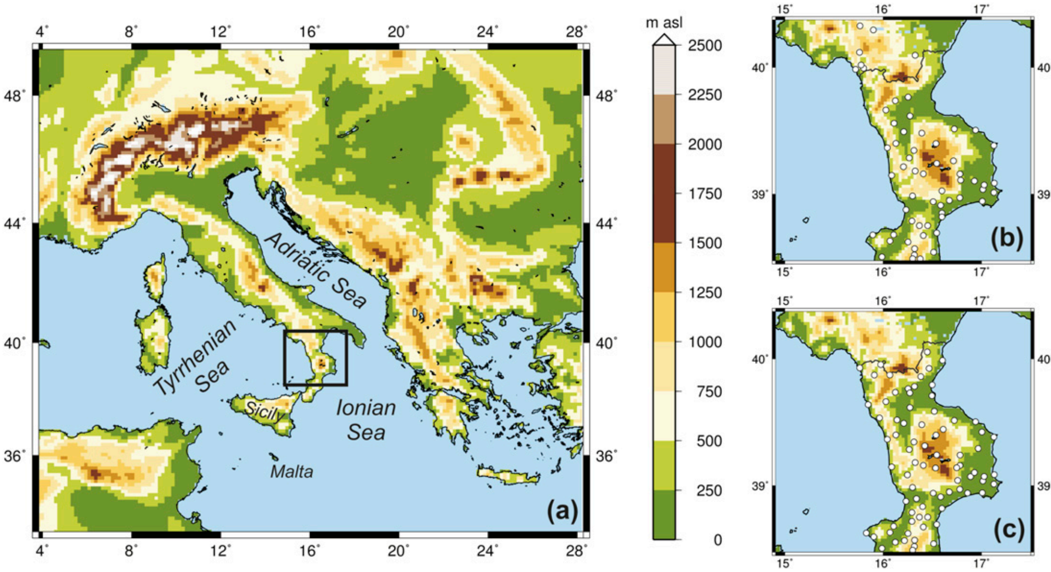

FIG. 1. (a) Outer domain, borders of the inner domain are also shown. (b) Inner domain, highlighting boundaries of the administrative region of Calabria, elevation and location of recording stations used in the period from October 2001 to September 2002. (c) As in (b), but for recording stations used in the period from November 2008 to January 2009.

experiments to SST fields. The latter experiments are an essential reference for a better understanding of the changes induced by different interpolation procedures.

In the following two sections, the data and the preliminary WRF parameterization analysis in northern Calabria are described (section 2), followed by the analysis of the impact of different SST fields on the WRF-derived precipitation patterns (section 3).

2. Data and methods

The Advanced Research WRF (ARW) Model, version 3.3.1, is used in two one-way nested domains: a large domain, with a 12.5 km (172 × 154 grid points) horizontal resolution covering the central region of the Mediterranean basin (32.6°–49.9°N, 3.1°–29.1°E; Fig. 1a), and a small domain, with a 2.5 km (95 × 90 grid points) horizontal resolution, covering an area (38.4°–40.5°N, 14.8°–17.6°E) corresponding mainly to central-northern Calabria in southern Italy (Figs. 1b,c). Calabria is a peninsula located in the center of the Mediterranean, oriented north–south, surrounded by the Tyrrhenian Sea (to the west) and the Ionian Sea (to the southeast). It is predominantly a mountainous region (with peaks over 2000 m), where orography and sea interactions affect the local climate. The time step of the model simulation is 60 s in the large domain, decreasing to 12 s in the small domain. Furthermore, the vertical structure of both domains consists of 44 levels, up to a 50-hPa pressure top (about 20 000 m). Initial and lateral atmospheric boundary conditions for continuous runs are given by the Interim ECMWF Re-Analysis (ERA-Interim; Dee et al. 2011), which uses different datasets for representing SST. Specifically, the National Oceanic and Atmospheric Administration (NOAA) Optimum Interpolation SST, version 2 (OISST2), is used from July to December 2001, while the National Centers for Environmental Prediction (NCEP) Real-Time Global (RTG) SST dataset is used from January 2002 to January 2009. Both datasets provide daily values with 0.5° resolution.

The special methodology developed here for SST field ingestion at daily time resolution does not rely on ERA-Interim but consists of a GIS-based external preprocessing of the original SST datasets (namely, NOAA OISST2 and NCEP RTG) by means of the following steps. First, the original SST grids are imported into the GIS. It is noteworthy that, different from ERA-Interim data, land values in these grids are not set to missing but are filled by a Cressman interpolation to produce a complete grid for possible interpolation to other grids. Second, the SST grids are resampled to the WRF domain cell size using the nearest neighbor technique. Third, the new SST grids are masked with previously defined sea grid points. Afterward, the new SST grids are directly ingested into the WRF lower boundary conditions files (which were created previously following the usual WRF preprocessing procedure) by replacing the existing SST grid cell by cell for every time step. For this task, the Python interface to the

TABLE 1. WRF configurations considered in this study and their acronyms. Microphysics (M) schemes: option 2 is for Purdue Lin, option 6 is for WSM6, and option 8 is for Thompson graupel. PBL (P) schemes: option 1 is for YSU scheme and option 2 for MYJ. Cumulus parameterization (C) schemes: option 1 is for Kain–Fritsch and option 3 for Grell–Dévényi ensemble.

	M2P1	M2P2	M6P1	M6P2	M8P1	M8P2	M2P2C3	M6P2C3
Microphysics	2	2	6	6	8	8	2	6
PBL	1	2	1	2	1	2	2	2
Cumulus parameterization	1	1	1	1	1	1	3	3

netCDF, version 4 (*netcdf4-python*), library is used. The strength of this method relies on direct reference to the original SST dataset, which can be masked considering the actual land grid points used in the WRF simulation. The same method is also used for selected ancillary data, namely, land cover and soil categories, which are replaced by more detailed datasets available for the small domain.

Our WRF parameterization analysis focuses on a very wet 3-month-long period (from November 2008 to January 2009). The same period will be used afterward for the analysis of modeled precipitation sensitivity to different SST representations and will be complemented by an additional drier 12-month-long period (from October 2001 to September 2002). Hence, the model hindcasts focus on extreme hydrological events because it is in these cases that differences among configurations are more pronounced.

The starting point for the selection of model physics options is the choice of parameterizations used by the Institute of Atmospheric Sciences and Climate–Italian National Research Council (ISAC-CNR; Lecce office) in its operational forecasts. These are the Thompson et al. (2008) microphysics scheme (a new bulk microphysical parameterization available within WRF, version 3.1), a modified version of the Kain–Fritsch scheme (Kain 2004) cumulus parameterization for the coarser grid and explicit convection for the finer grid (since cumulus parameterizations are theoretically only valid for grid sizes >5–8 km below which the model can resolve the convective eddies itself; Skamarock et al. 2008), the Rapid Radiative Transfer Model (RRTM) for longwave radiation based on Mlawer et al. (1997), the Dudhia (1989) scheme for shortwave radiation, the unified Noah land surface model, and the prognostic turbulent kinetic energy Mellor–Yamada–Janjić (MYJ) scheme for the parameterization of turbulence in the planetary boundary layer (PBL; Janjić 2002). Furthermore, the *sst skin* option is used. This option allows us to increase SST daily time resolution, reproducing the SST diurnal variation from the energy budget over the sea surface and accounting for the cooling effect of longwave radiation and the warming effect of solar insolation (Zeng and Beljaars 2005).

Since the main interest of this study is precipitation, the parameterization analysis mainly focuses on the microphysics schemes as they explicitly include precipitation processes. Since the cumulus parameterization is switched off in the inner domain, they play an even more relevant role in our specific case. The Thompson et al. (2008) scheme is compared to two complex schemes that both include six classes of hydrometeors: 1) the Purdue Lin scheme (Chen and Sun 2002), which is a relatively sophisticated scheme and is most suitable for use in research studies (Skamarock et al. 2008), and 2) the WRF single-moment 6-class (WSM6) microphysics scheme, which refers to the works of Lin et al. (1983) and Rutledge and Hobbs (1984) for the graupel-related terms, but with a revised ice-phase behavior (Hong et al. 2004) as well as a new method for representing mixed-phase particle fall speeds for the snow and graupel particles (Dudhia et al. 2008). Additionally, each of the three microphysics parameterizations is tested with a different PBL scheme, which

TABLE 2. Statistics and performance indices of tested parameterizations (inner domain) for both accumulated precipitation values in the cells corresponding to gauging stations and mean daily precipitation series; wet period is from November 2008 to January 2009.

		Obs	M2P1	M2P2	M6P1	M6P2	M8P1	M8P2	M2P2C3	M6P2C3
Whole period	Mean (mm)	743.5	791.6	738.1	745.9	710.4	718.7	585.5	699.6	660.8
	Std dev (mm)	257.8	256.1	243.9	239.7	239.6	246.6	211.2	257.0	258.3
Linear regression	Slope	—	0.48	0.49	0.53	0.53	0.47	0.42	0.33	0.40
	Intercept	—	433.3	370.9	347.7	313.3	372.2	269.4	455.5	363.4
	r	—	0.49	0.52	0.57	0.57	0.49	0.51	0.33	0.40
Daily	E	—	0.66	0.66	0.69	0.68	0.36	0.64	0.48	0.55
	Wet days	71	72	72	74	72	71	67	76	75

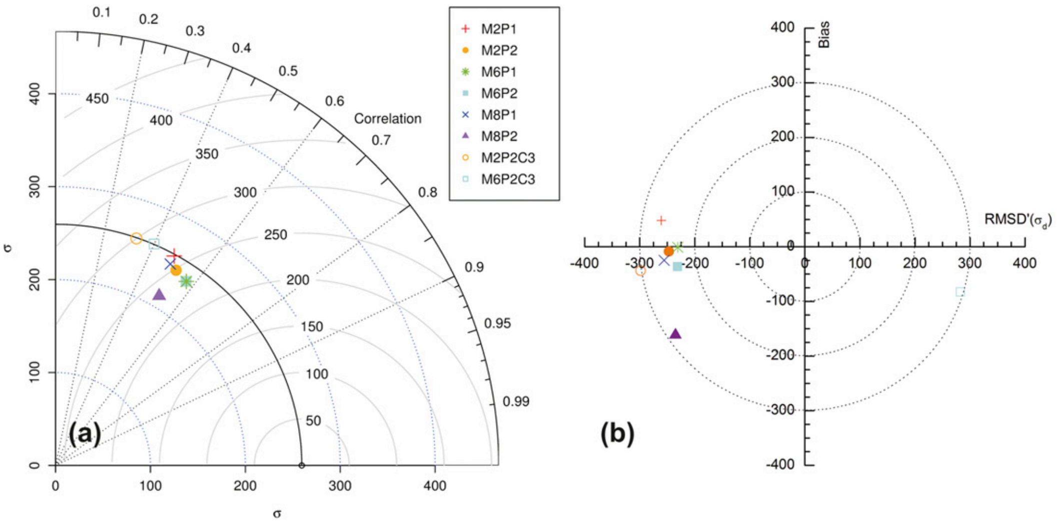

FIG. 2. (a) Taylor diagram and (b) target diagram related to accumulated precipitation values in the period from November 2008 to January 2009 (inner domain). By definition of the target diagram, points on the left side of the diagram indicate that std dev differences between simulated and observed mean values series are negative.

provides atmospheric tendencies of temperature, moisture (including clouds), and horizontal momentum in the atmospheric column. The alternative scheme to MYJ is the Yonsei University (YSU) PBL scheme (Hong et al. 2006), a diagnostic nonlocal scheme that is frequently used in previous WRF applications in southern Italy (e.g., Miglietta and Regano 2008; Bertotti et al. 2009; Mastrangelo et al. 2011). The different WRF configurations used are summarized in Table 1.

Validation of WRF parameterizations

The wet period from November 2008 to January 2009 in northern Calabria was characterized by very intense rain events, with a recurrence interval equal or longer than 20–50 years in many areas. Accumulated precipitation readings at some stations were higher than 1300–1400 mm. Modeled precipitation fields obtained by simulations with a spinup of 1 month are compared to observed values from 79 available rain gauges ranging from 5 to 1730 m MSL (Fig. 1c).

Several metrics are used in order to assess the performance of the configurations. Concerning accumulated precipitation amounts, Table 2 compares observed and simulated average values and average standard deviations for the gauging stations, together with slope and intercept of the scatterplots of observed and simulated precipitation. The Pearson correlation coefficient *r* is also given as a measure of linear correlation of simulated and observed accumulated values. Furthermore, Fig. 2 shows the Taylor diagram of spatial correlation and variance (Taylor 2001) and a target diagram (Jolliff et al. 2009). The Taylor diagram graphically summarizes the matching between simulations and observations, combining their correlation, their centered RMS

TABLE 3. Statistics and performance indices of tested parameterizations (inner domain) for both accumulated precipitation values in the cells corresponding to gauging stations and mean daily precipitation series; dry period is from October 2001 to September 2002. The corresponding dry days row shows the percentage of the total number of observed dry days (i.e., 165) correctly simulated by the WRF configurations.

		Obs	M2P1	M2P2	M6P1	M6P2	M8P1	M8P2
Whole period	Mean (mm)	832.7	972.8	859.0	975.2	855.2	799.8	687.1
	Std dev (mm)	296.6	309.9	269.8	370.5	312.5	295.8	222.7
Linear regression	Slope	—	0.63	0.59	0.71	0.63	0.64	0.45
	Intercept	—	444.9	364.2	369.8	334.5	265.1	314.4
	r	—	0.61	0.65	0.57	0.59	0.64	0.60
Daily	*E*	—	0.29	0.47	0.35	0.47	0.49	0.55
	No. of dry days	165	142	148	127	130	147	154
	Corresponding dry days	—	73%	75%	67%	68%	73%	77%
	Dry spells max length	17	8	14	7	8	7	14

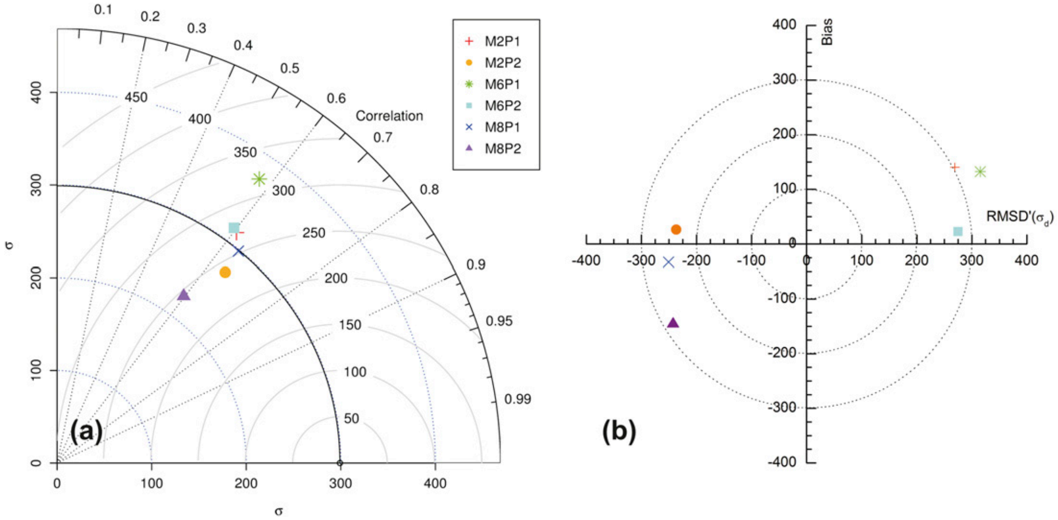

FIG. 3. As in Fig. 2, but for the period from October 2001 to September 2002.

difference (RMSD′), and the amplitude of their variations (represented by the standard deviations). Since a drawback of the Taylor diagram is that the bias is not accounted for, the accompanying target diagram integrates information about the statistical performance of the models (in Fig. 2b the RMS differences are represented by the distance of the points from the target).

Average daily rain series are also analyzed through the Nash–Sutcliffe (Nash and Sutcliffe 1970) coefficient E, which assesses the time correlation of precipitation events and the predictive power of different WRF parameterizations (higher model efficiency is represented by E values closer to 1). Furthermore, the number of wet days, that is, the days with precipitation in the analyzed area, is considered (Table 2).

In the wet period, results are generally comparable (Table 2). Except for parameterization M8P2, both mean and standard deviation biases are well below 10%, and for M2P2 and M6P1 they are even below 1%. Scatterplots' slope and intercept indicate that a slightly better behavior is achieved using M6P1 and M6P2, which exhibit the best regression curves and Pearson correlation coefficient r. The diagrams in Fig. 2 confirm the generally weak differences between the parameterizations, with M2P2 and M6s being very similar. The daily comparison also shows a quite similar performance, with the number of wet days well reproduced by all models and E values ranging from 0.64 to 0.69 for all but M8P1. However, monthly accumulated values (not shown) suggest that M2P2 and M6P2 are the only parameterizations capable of describing, with no relevant bias, the overall increase in monthly values from November to January, while M6P1 significantly overestimates it in December and underestimates it in the other months.

Based on these findings, a sensitivity analysis with cumulus parameterization schemes other than the Kain–Fritsch scheme (which is based on a mass flux approach) is conducted for the M2P2 and M6P2 parameterizations. Even though the convective parameterization is only applied to the outer domain, this approach is relevant for the simulation of precipitation fields because it is related to moist convection, representing within the hydrological cycle the effects of subgrid-scale processes on the grid variables (Stensrud 2007). Hence, the Grell–Dévényi ensemble scheme (Grell and Dévényi 2002) is used as an alternative approach. This scheme is an ensemble parameterization where several closures and parameters are varied and the ensemble mean tendencies are then returned to the numerical model. It was adopted previously by Schurmann et al. (2009) in their study with WRF-Chem in northern Calabria. As shown in both Table 2 and Fig. 2, using the Grell–Dévényi cumulus parameterization for the outer domain negatively affects the simulation in the inner domain.

The analysis for the wet period is now extended for the dry period from October 2001 to September 2002, that is, a drought year in northern Calabria (Mendicino et al. 2008), preceded by a reduction of rainfall in the previous years and characterized by lower-than-average precipitation, especially in the period from January to March 2002. Also for this simulation a spinup of 1 month is considered, and modeled precipitation fields are compared to observed data from 60 rain gauges ranging from 5 to 1315 m MSL (Fig. 1b). Performance assessment metrics are similar to the wet period, except that in place of the number of wet days the complementary number of dry days is considered, together with the percentage of observed dry days correctly simulated and

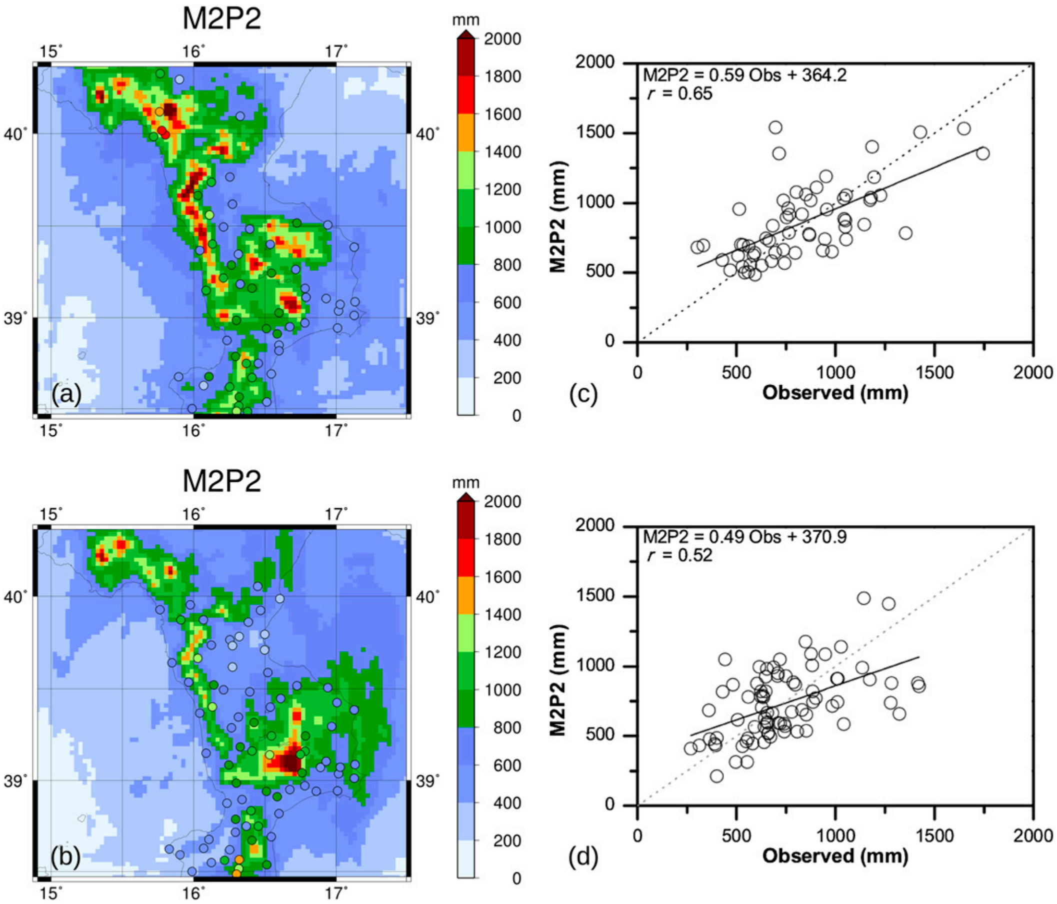

FIG. 4. Maps of simulated precipitation fields for configuration M2P2 in the period from (a) October 2001 to September 2002 and (b) November 2008 to January 2009 and (c),(d) related scatterplots of observed vs simulated precipitation. Colored circles represent observed precipitation values for each recording station available.

the maximum length of observed and simulated dry spells (Table 3). Mean and standard deviation differences with respect to observations are both below 10% only for M2P2, M6P2, and M8P1. However, the Taylor diagram (Fig. 3a) points out that the best performance in terms of spatial correlation and RMS differences is provided by M2P2. The analysis of the daily series suggests a better performance for M8P2. However, this configuration is affected by an overall negative bias. As before, M2P2 shows good performance with respect to the other parameterizations, especially in reproducing the dry spell characteristics.

In summary, no single configuration strongly predominates in terms of performance indices in both the wet and the dry period. However, M2P2 is the best configuration in the dry period, considering both the whole year and daily series comparisons. It also shows better or comparable performance with the other configurations in the wet period and exhibits the lowest bias in precipitation overall. Hence, M2P2 is considered as the reference parameterization for further analysis of precipitation patterns sensitivity to different SST representations. To illustrate the reliability of M2P2 precipitation patterns, Fig. 4 shows the georeferenced observed accumulated precipitation values for each station for the wet and the dry period, superimposed on the maps of the M2P2 simulated fields, together with related scatterplots of observed versus simulated precipitation.

3. SST representation impact on precipitation patterns

The chosen period for analyzing SST representation effects on precipitation patterns in continuous long-term simulations is the wet period from November 2008 to January 2009, characterized by many significant rain events. The control simulation M2P2 is modified by changing the SST lower boundary condition in different ways. The main difference is the following: in the control

TABLE 4. Description of different SST representations and relative configurations IDs.

Config. ID	Description
SST0	ERA-Interim SST fields are interpolated using 16-point overlapping parabolic interpolation or 4-point bilinear interpolation. These methods are the most complex available in WPS as they require 16 or 4 valid source points, respectively. Hence, along coastlines missing values can arise. This problem can be solved in different ways, the easiest being to fill missing data with a constant value. The constant value chosen is the average SST value in the analyzed period from Nov 2008 to Jan 2009 (i.e., 290.5 K for the large and 290.0 K for the small domain).
SST1	ERA-Interim SST fields are interpolated using 16- or 4-point average interpolation, which are simpler interpolation methods working even with only one valid source data point. WPS allows the user to list more than one interpolation method, so that if it is not possible to employ the *i*th method in the list, the $(i + 1)$th method will be employed, and so on. Hence, it would be possible to list a complex interpolation method, like the ones used with SST0 configuration, followed by a simpler one. However, SST1 configuration exclusively uses either a 16- or 4-point average interpolation in order to specifically assess their effects on precipitation patterns.
SST2	ERA-Interim skin temperature (TSK) fields are interpolated using 16-point overlapping parabolic interpolation or 4-point bilinear interpolation. TSK fields contain both SST and LST fields instead of considering only SST; hence, missing values do not arise. However, since a smooth transitional function is used, near-coastal SST values are affected by LST values.
SST3	ERA-Interim SST fields are interpolated using 4-point bilinear interpolation and, if not possible, 4-point average interpolation. This configuration differs 1) from SST0, because it is allowed to use less complex interpolation methods when needed; 2) from SST1, because more complex interpolation methods are allowed and preferred when applicable; and 3) from SST2 because, since only SST data are considered, the physical sea–land transitional barrier is taken into account, allowing a sharp transition from SST to LST.
M2P2 + ε	The SST fields used in M2P2 configuration are uniformly increased by a value $\varepsilon = 0.5$ K.
M2P2 − ε	The SST fields used in M2P2 configuration are uniformly decreased by a value $\varepsilon = 0.5$ K.

simulation, SST fields are derived directly by the original SST datasets (namely, NOAA OISST2 and NCEP RTG), where land values are filled by a Cressman interpolation, but in the new configurations, SST fields are derived from the ERA-Interim dataset, where (as it was hinted at in section 2) land grid points are filled with missing values and need to be dealt with by means of spatial interpolation techniques. Several available interpolation options in the WRF Preprocessing System (WPS) are used to ingest SST fields into the WRF input files. These different SST representations, leading to six new configurations—SST0, SST1, SST2, SST3, M2P2 + ε, and M2P2 − ε—are described in detail in Table 4. The latter two configurations serve as reference to compare the variability of the SST0–SST3 configurations to a simple decrease/increase of SST values by 0.5 K. According to NCEP ensemble verifications of the RTG SST analysis with independent data (available at http://polar.ncep.noaa.gov/sst/rtg_low_res/Verifcounts.html), a variation of $\varepsilon = \pm 0.5$ K is a reasonable perturbation value of the same order of magnitude as the RMSD of the NCEP verifications.

Figure 5 displays the average SST values for the outer domain for the entire period analyzed. SST patterns in M2P2, SST1, and SST3 configurations are quite similar, with small changes in the smoothing of the contour lines caused by the different interpolation methods. Average SST values are almost identical (289.9 K for SST1, 289.8 K for SST3, and 290.2 K for M2P2), and cell by cell comparisons show that differences slightly higher than 1 K (due to SST1 and SST3 underestimates) can be found only sporadically in the Marmara Sea (eastern border of the outer domain, at about latitude 40°N) or close to the Aegean and southern Tyrrhenian coasts. In contrast, the SST patterns in the SST0 configuration show that the average constant value chosen to fill missing values is not reliable for most parts of the coastline. Differences with respect to the control simulation vary from −2.5 K in the south to +5.0 K at the Black Sea coasts (although the average value is 290.2 K and is equal to M2P2). Finally, the average SST field in the SST2 configuration is strongly influenced by the distance from the coast. Since the analysis is performed during winter months, lower values of land surface temperature (LST) than SST lead to an underestimation of up to 7–10 K in some cells located near the Greek or northern Italian coast. In these areas, on some very cold days (maps not shown) SST values can even fall below 273.15 K. Average SST values decrease along the Calabrian coastline by 3–5 K. The overall average SST value for the SST2 configuration is 289.4 K, 0.8 K less than M2P2.

The sensitivity analysis of precipitation patterns to SST fields is performed only for the inner domain. In Table 5, the new configurations are compared to observational data. Accumulated values for the full period as well as mean daily precipitation series are considered. The variability of statistical and performance indices of the SSTx and M2P2 ± ε configurations is of the same order as in the previous parameterization analysis (see

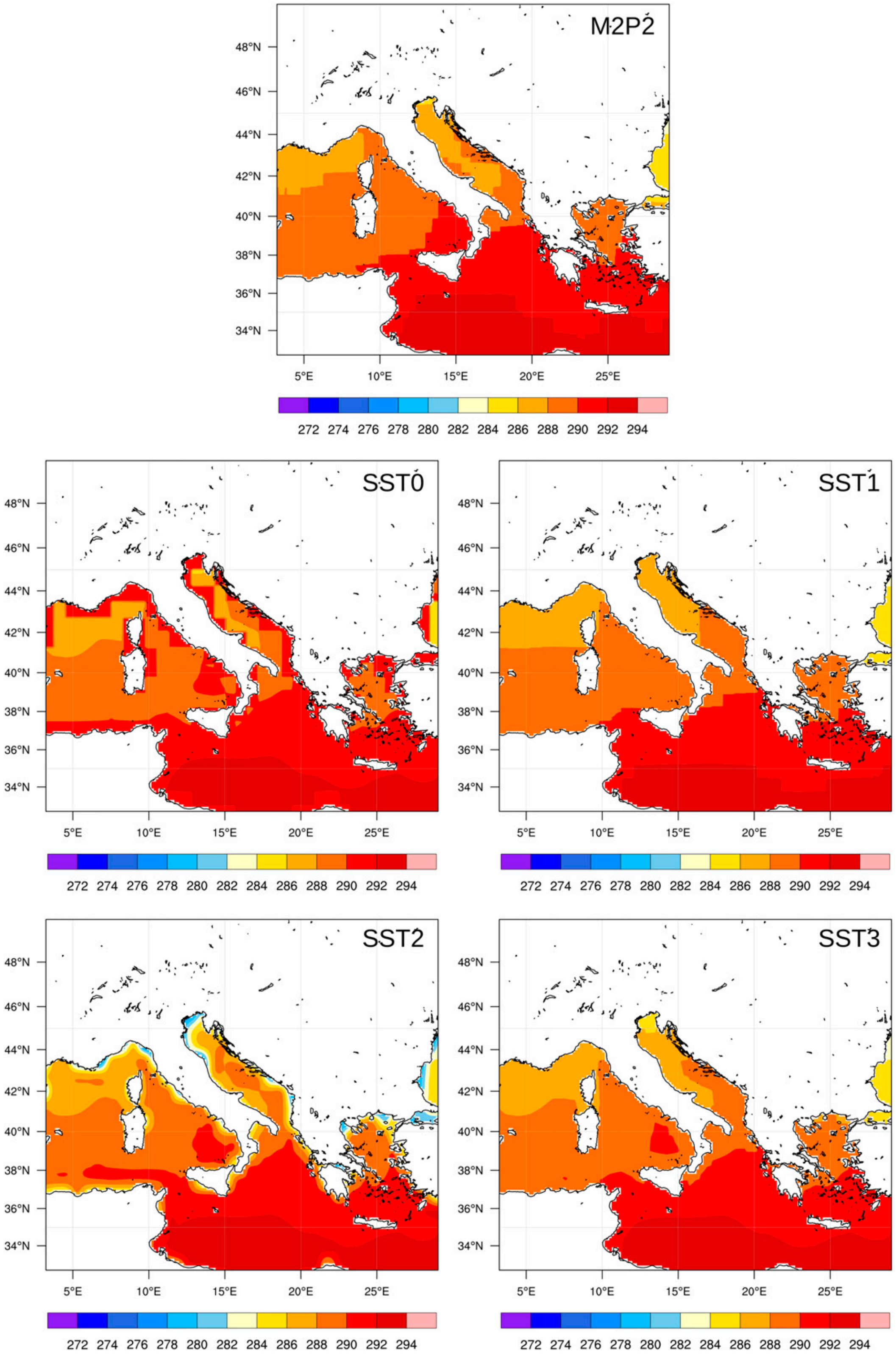

FIG. 5. Average (from November 2008 to January 2009) SST values (K) for M2P2, SST0, SST1, SST2, and SST3 configurations.

TABLE 5. Statistics and performance indices for M2P2, M2P2 + ε, M2P2 − ε, SST0, SST1, SST2, and SST3 configurations with respect to observed data (inner domain) from November 2008 to January 2009.

		Obs	M2P2	M2P2 + ε	M2P2 − ε	SST0	SST1	SST2	SST3
Whole period	Mean (mm)	743.5	738.1	729.4	740.1	669.3	737.2	712.5	730.2
	Std dev (mm)	257.8	243.9	229.1	275.4	200.1	270.8	261.1	263.4
Linear regression	Slope	—	0.49	0.46	0.62	0.44	0.45	0.51	0.43
	Intercept	—	370.9	384.3	278.7	340.4	404.2	332.5	407.8
	r	—	0.52	0.53	0.58	0.57	0.42	0.51	0.43
Daily	E	—	0.66	0.65	0.55	0.71	0.62	0.58	0.59
	Wet days	71	72	72	74	70	74	69	76

Table 2). More precisely, mean values are quite similar and biases almost always below 10% (except for SST0 with a 10% underestimation). Hence, when considering the whole period, the effects of the SST representation on precipitation are small.

The SSTx and M2P2 ± ε configurations are also directly compared to the control simulation M2P2. Maps of percentage differences of accumulated precipitation are displayed in Fig. 6. Even though for all configurations a certain clustering is evident, no general trend of spatial over- or underestimation can be inferred (clusters of over- and underestimation are related to single events, some of which will be explained in subsequent paragraphs). Since accurate estimates of precipitation over land are of paramount importance for manifold practical applications, a more detailed analysis focuses on the differences over land cells within the Calabrian territory (Table 6; Calabrian boundaries are shown in Figs. 1b,c). Linear regression equation parameters and r values confirm that single cell values are generally similar. Differences in mean accumulated values are also within ±20 mm (except for SST0 with −72.6 mm). However, contrary to what is expected, two of the configurations with highest average SST values, that is, M2P2 + ε and SST0, have lower-than-average precipitation values, while M2P2 − ε shows the highest mean accumulated precipitation over land. An explanation of this somewhat unexpected behavior can be found by shifting the analysis from a space to a time scale.

Figure 7 shows the daily evolution of mean SST in the inner domain (Fig. 7a) together with the daily accumulated mean precipitation in cells within the Calabrian territory (Fig. 7b). Further, relative differences in daily precipitation of the other configurations with respect to M2P2 are displayed (Fig. 7c). Figure 7b also shows, as a reference, accumulated observed daily precipitation (in gray) as calculated by averaging daily interpolated maps of observed data over the same area. Compared to the control simulation, SST average values in SST0 are underestimated for the first half of the analyzed period and overestimated afterward. SST2 values are almost always lower than control simulation values by about 2 K, while SST1 and SST3 are similar to M2P2 − ε. The temporal evolution of differences in SST is not reflected in the accumulated precipitation: until 27 December 2008, only small differences can be found (except for M2P2 + ε in mid-November). From 27 to 29 December 2008 and on 9 January 2009, however, Fig. 7c shows significant differences in daily precipitation. The overall underestimation of SST in the SST0 configuration is largely caused by these events. In the same manner, the differences in accumulated values at the end of the analyzed period for all other configurations can be attributed to single events rather than to a continuous deviation. In fact, Fig. 7 shows that for specific events SST representation can deeply affect precipitation patterns over land.

Table 7 summarizes spatially averaged observed and simulated daily precipitation values for these events. It is noteworthy that the control simulation does not always provide the best results with respect to the observations. In the following, the events of 9 January 2009 and of 27–29 December 2008 are analyzed in detail.

a. The 9 January 2009 event

On 9 January 2009, the SST fields of the outer domain of the different configurations show patterns and features similar to the SST fields averaged for the whole period shown in Fig. 8. The M2P2 mean SST value (288.3 K) is about 0.3 K higher than that of SST1 and 0.4 K higher than that of SST3, with localized peaks from +2 to +3 K along the central Adriatic and southern Tyrrhenian coastlines. Because of the LST effects discussed above, the mean SST value of the SST2 configuration is lower (287.5 K), with values around Calabria being 6–7 K colder than M2P2. Conversely, the SST0 mean value is 288.9 K and similar to M2P2 + ε. As a comparison, 2.2-km-resolution satellite observations [Medspiration level 4 (L4) Ultra-High Resolution foundation SST (SSTfnd) from the Medspiration Project by the Centre European Remote Sensing (ERS) d'Archivage et de Traitement (CERSAT), Institut Français de Recherche

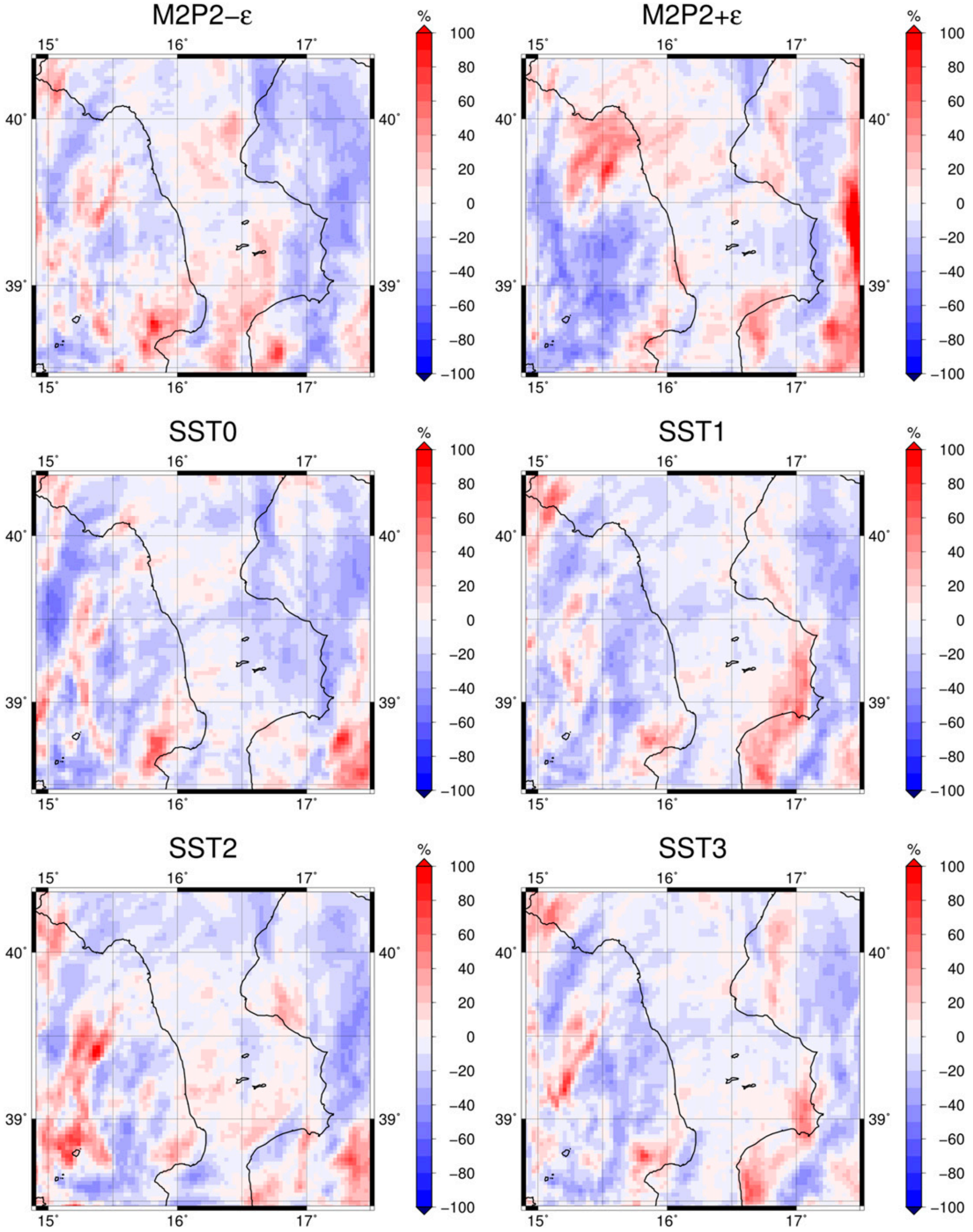

FIG. 6. Accumulated precipitation differences (%) between M2P2 − ε, M2P2 + ε, SST0, SST1, SST2, and SST3 configurations and M2P2.

pour L'Exploitation de la Mer (IFREMER)] are also displayed. On average, these observations show slightly higher SST values (mean SST equal to 288.6 K) than the SST*x* configurations, especially in the Tyrrhenian Sea and the western Mediterranean basin.

The different SST fields lead to the daily precipitation patterns shown in Fig. 9. The intensities of simulated rain events are generally comparable, but they are concentrated over different areas within the domain. Specifically, in configurations with higher SST values (M2P2 + ε and SST0), precipitation is generated mainly over the sea, while in configurations with lower SST values (namely, M2P2 − ε, SST1, SST2, and SST3), patterns are more clearly affected by orographic effects.

TABLE 6. Average values, std dev, and parameters of linear regressions with respect to M2P2 and Pearson correlation coefficient related to all land cells within the Calabrian territory.

	M2P2	M2P2 + ε	M2P2 − ε	SST0	SST1	SST2	SST3
Mean (mm)	809.7	797.8	828.9	737.1	805.0	798.2	794.2
Std dev (mm)	321.5	304.6	387.0	288.8	341.2	341.8	336.3
Slope	—	0.91	1.14	0.86	1.02	1.04	1.01
Intercept	—	61.0	−90.7	39.2	−17.4	−40.0	−26.9
r	—	0.96	0.94	0.96	0.96	0.97	0.97

The control simulation, having intermediate SST values, also shows an intermediate pattern that fits very well to the observed data (colored circles in the maps).

Synoptic conditions leading to the 9 January 2009 event are characterized by a large anticyclone extending from the Atlantic Ocean to Russia, which hits weather fronts generated by northwestern Africa low-pressure systems, in turn moving toward high-pressure systems located in eastern Europe and Anatolia. In this context, a minimum in sea level pressure of 1012 hPa south of

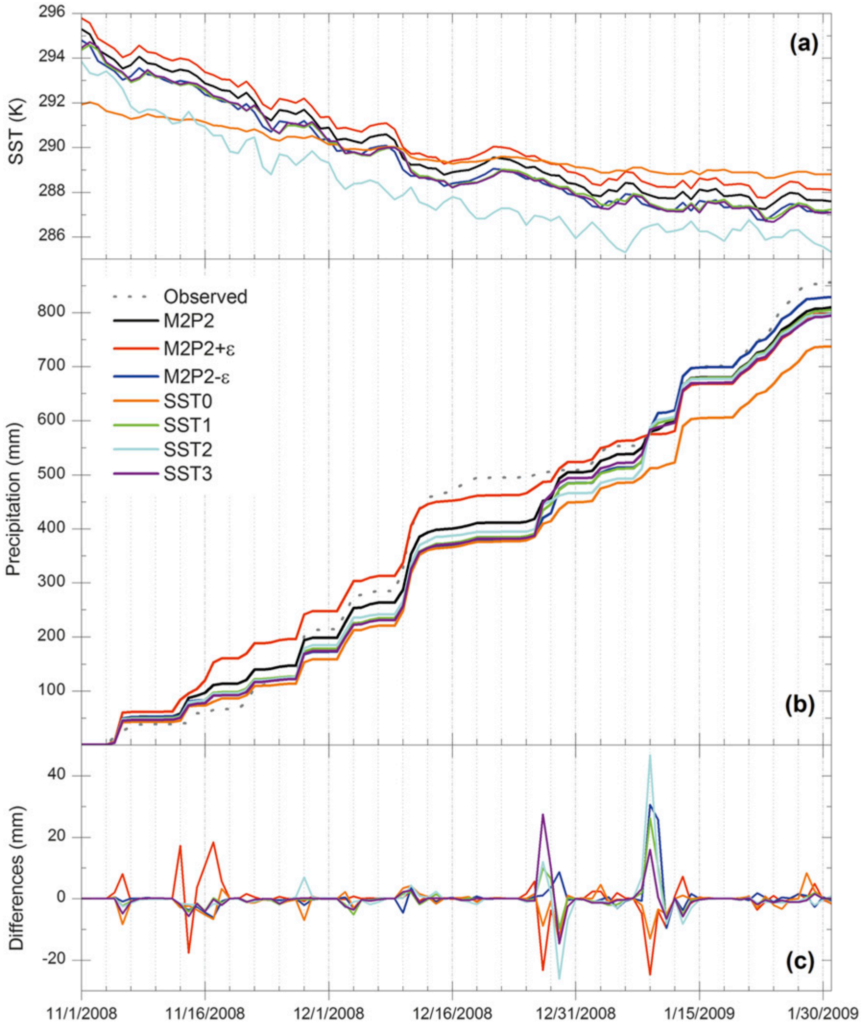

FIG. 7. (a) Daily evolution of mean SST in the inner domain (period from November 2008 to January 2009), (b) daily evolution of accumulated mean precipitation in the grid cells within the Calabrian boundaries, and (c) daily precipitation differences of all other configurations with respect to M2P2.

TABLE 7. Spatially averaged daily precipitation values (mm) in the cells within the Calabrian boundaries for 27 and 29 Dec 2008 and 9 Jan 2009.

	Spatially interpolated from observations	M2P2	M2P2 + ε	M2P2 − ε	SST0	SST1	SST2	SST3
27 Dec 2008	3.48	33.37	10.09	34.38	24.44	43.30	45.35	60.81
29 Dec 2008	1.52	36.31	24.07	44.96	22.33	26.60	10.15	21.71
9 Jan 2009	31.50	29.93	5.23	60.51	16.88	56.07	76.71	45.87

Malta is apparent in each configuration at 1200 UTC 8 January 2009 (Fig. 10). The SST boundary conditions of the different configurations affect the tracks of the pressure minima. In particular, Fig. 10a shows that the M2P2 + ε trough moves faster than in M2P2 and M2P2 − ε and eventually turns toward the Ionian Sea. This is because of an increase in available energy due to higher SST temperatures and stronger winds, probably produced by an increase in air temperature gradient. In the afternoon of 9 January, pressure minima of M2P2 and M2P2 − ε, on the other hand, are located over the Tyrrhenian Sea (the lower the SST values, the more westerly the location of the trough). All SSTx configurations follow this pattern (Fig. 10b). Specifically, when the SST0 trough reaches the Sicilian coastline (hence, when it encounters higher SSTs), it also speeds up and follows a track similar to M2P2 + ε. The troughs in SST1, SST2, and SST3 move toward the Tyrrhenian Sea, but their final position is slightly more westerly than in M2P2.

Depending on the track and position of the pressure minima, the water vapor distribution in the inner domain changes significantly. Figure 11 shows that the north–south-oriented shape of Calabria splits the wet air mass moving northward during the night hours between 8 and 9 January 2009. The amount of water vapor moving to the east or to the west of the peninsula is correlated to the tracks of the pressure minima, hence to the SST values. This is also confirmed by Fig. 12, which shows that the column integrated water vapor (IWV) of the SSTx configurations is distributed similarly to M2P2. Despite these generally consistent findings in the outer domain, a more detailed analysis in the inner domain is needed for a better understanding of the differences in precipitation patterns shown in Fig. 9.

The inner domain is one-way nested in the outer domain. Its finer resolution and, more specifically, its more detailed terrain elevation with higher peaks (closer to reality) are essential for modeling orographic precipitation events. As for the pressure minima in the outer domain, IWV maxima are tracked in the inner domain, starting at 0000 UTC 9 January 2009 with a time interval of 3 h (Fig. 13). To facilitate the interpretation of the maps, only IWV maxima higher than an approximate threshold of $20\,\mathrm{kg\,m^{-2}}$ are shown. Figure 13a reveals that, although at the first time step an IWV maximum is located over the Tyrrhenian Sea also for M2P2 and M2P2 + ε, in the following hours only the M2P2 − ε IWV maxima are tracked. In the Ionian Sea, M2P2 and M2P2 − ε tracks are not far from each other, but IWV maxima values are always higher for M2P2. Similar to the outer domain, the SST0 track is closest to M2P2 + ε, while SST1, SST2, and SST3 show an intermediate behavior between M2P2 and M2P2 − ε (Fig. 13b).

The presence of two peaks in the Ionian and the Tyrrhenian Seas is an indicator for the different spatial distribution of wet air masses. With predominant southeasterly winds (see Figs. 11, 12, which show the 10-m wind intensity and direction), high values of IWV over the Tyrrhenian Sea suggest that water vapor flux from the Ionian Sea is crossing Calabrian orography. The example shown in Fig. 14 at 0200 UTC 9 January clearly illustrates the dynamics. Besides providing examples of IWV patterns, maps in the first row of Fig. 14 also show 10-m wind directions, which approximate low-level wind directions. The maps highlight that, because of the different distributions of the pressure minima, in M2P2 − ε winds run up against orographic features at the center of the domain, while in M2P2 + ε they are almost parallel to them (intermediate behavior for M2P2). Corresponding cross sections (including one of the main peaks of the massif) show an increase of water vapor mixing ratio for M2P2 − ε. Starting from the eastern border of the cross section to the windward slope and further to the leeward slope, higher values of water vapor mixing ratio are found than for M2P2 and M2P2 + ε. Orographic waves are also evident in the M2P2 − ε cross section, while the trend in water vapor mixing ratio from east to west is clearly descending in the M2P2 + ε cross section.

In the M2P2 − ε map in Fig. 14, two points [land (L) and sea (S)] are tagged. For these two points, skew T–log$p$ diagrams are generated for M2P2 − ε, M2P2, and M2P2 + ε (Fig. 15). The most important feature in these diagrams is the distance between temperature and dewpoint temperature lines. Regarding the L point, M2P2 − ε low levels are almost saturated, while M2P2 and M2P2 + ε are drier. For the S point, the situation is reversed: the

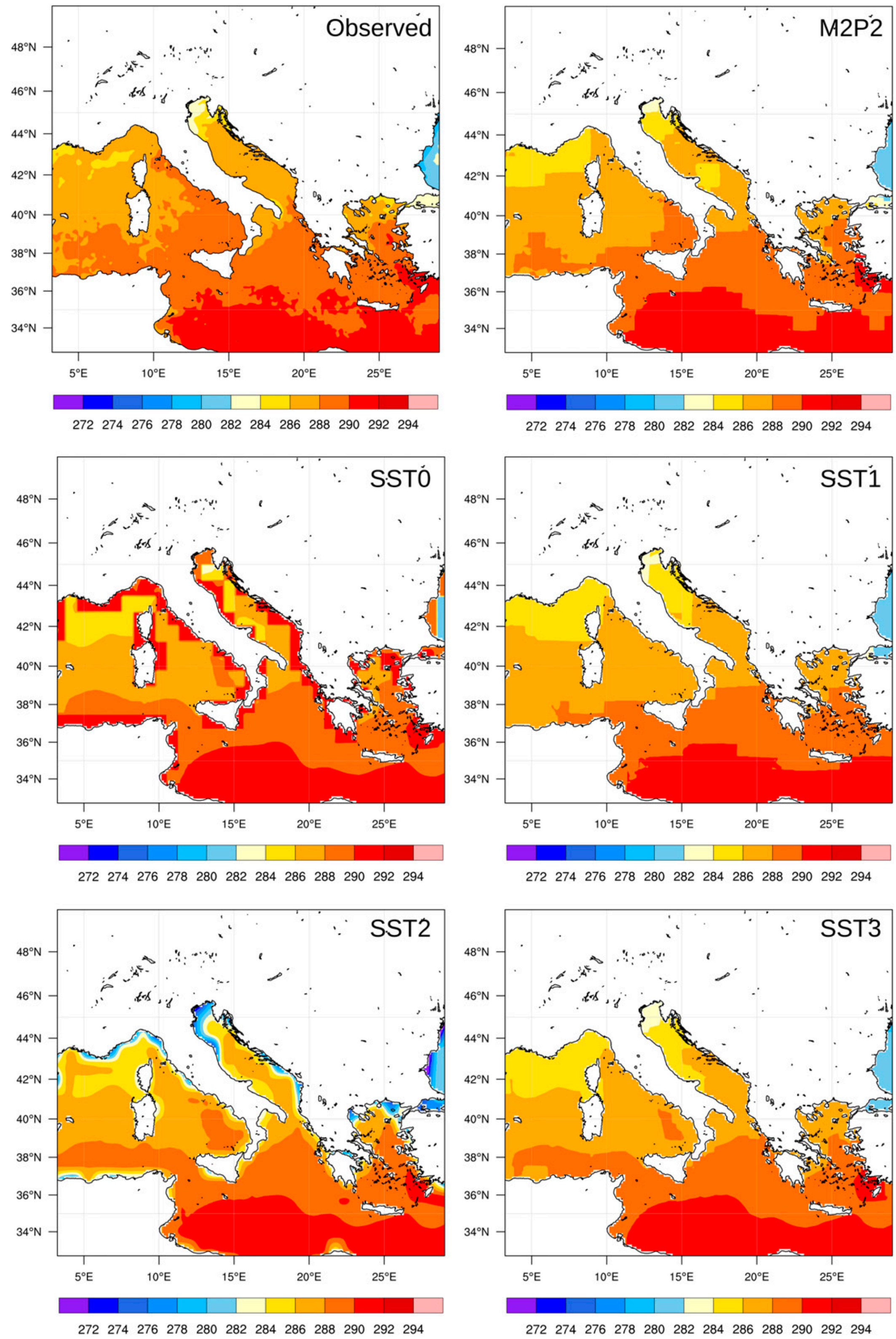

FIG. 8. Average SST values (K) on 9 Jan 2009 from high-resolution satellite data (observed) and for M2P2, SST0, SST1, SST2, and SST3 configurations.

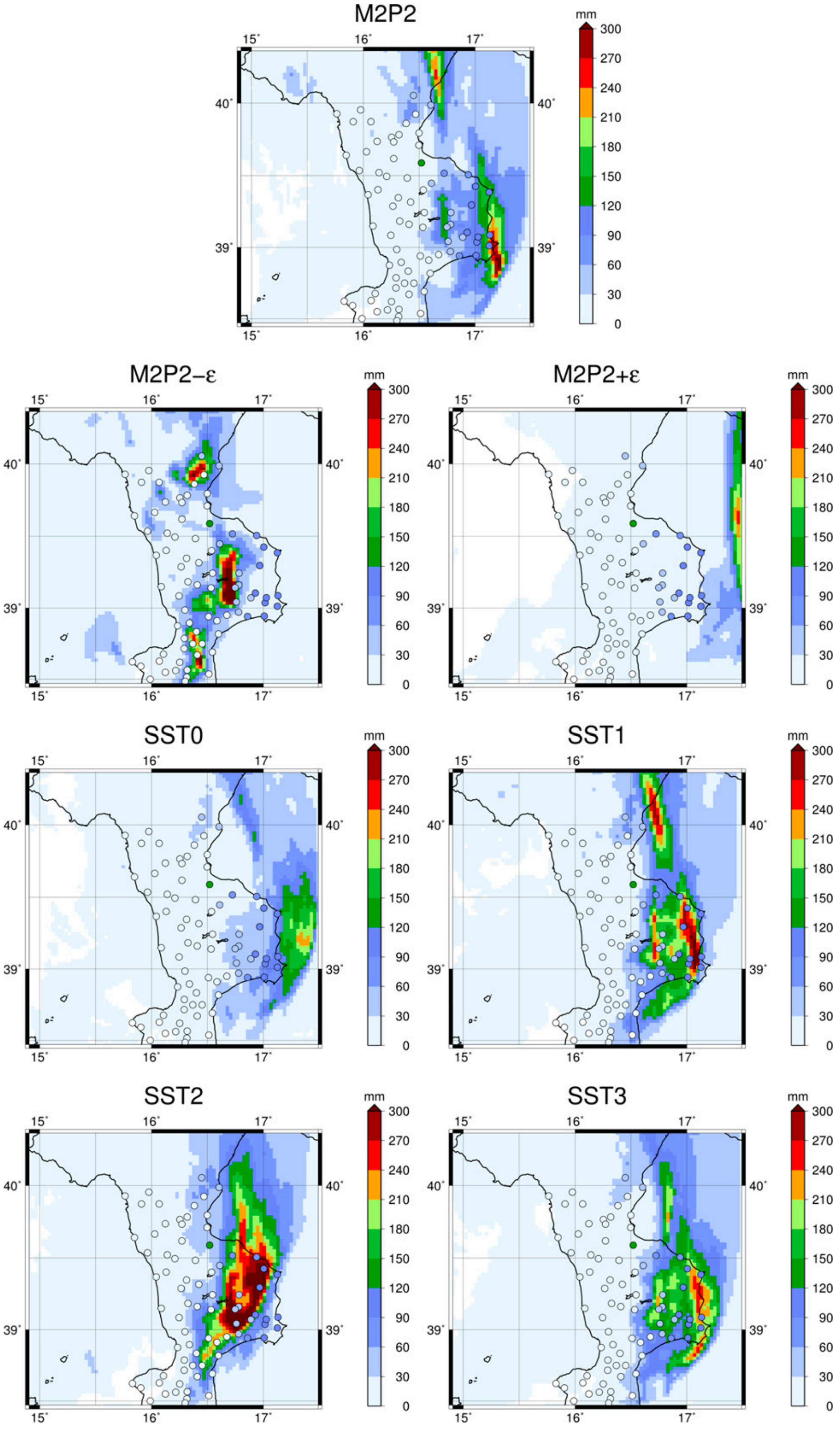

FIG. 9. Daily precipitation patterns in the inner domain on 9 Jan 2009. Colored circles in the maps represent observed precipitation values for each recording station available.

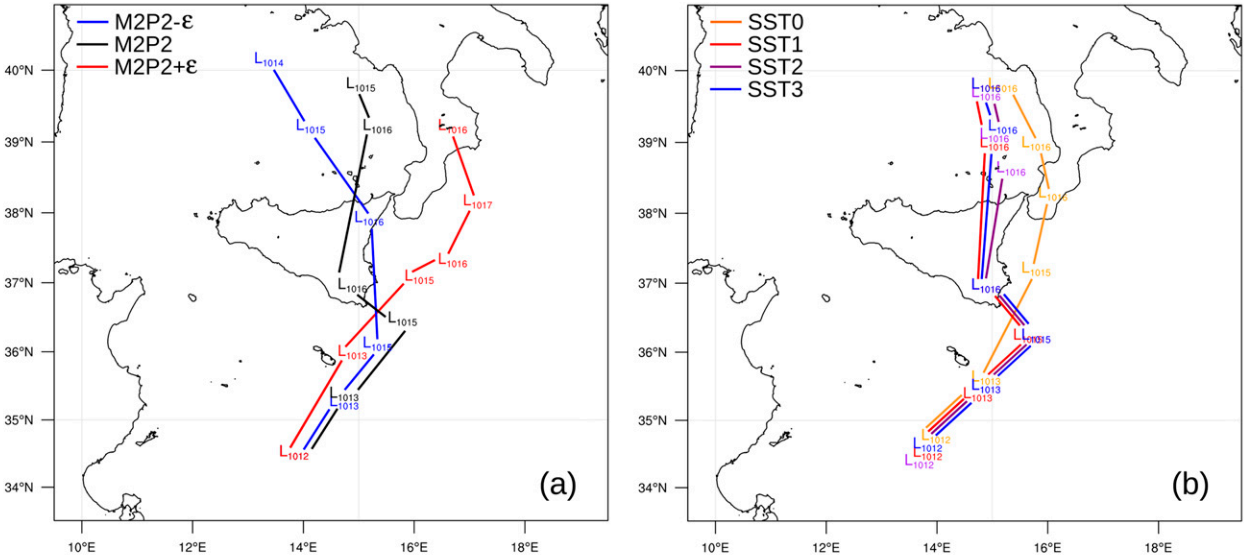

FIG. 10. Tracks of pressure minima for the different configurations calculated from the outer domain. Time steps considered are 1200 and 1800 UTC 8 Jan and 0000, 0600, 1500, and 2100 UTC 9 Jan.

M2P2 + ε profile is even saturated up to 7-km height. Derived CAPE values are always low (highest value of 276 J kg^{-1} for M2P2 − ε and S point). Maximum CAPE values of about 1000–1200 J kg^{-1} are achieved at the beginning of the analyzed event (i.e., on 8 January morning/afternoon) offshore (south and west of Malta).

The analysis of the 9 January event is completed by quantifying water vapor flux across the topography located at the center of the domain for all the simulations (Fig. 16). This methodology is proposed by Smith et al. (2010), who defined the vertically integrated horizontal water vapor flux Q_{flux} (kg m^{-1} s^{-1}) at each grid point along the edge of a box as

$$Q_{\text{flux}} = \frac{1}{g}\int q_v V_n \, dp\,, \qquad (1)$$

where g is the gravitational acceleration (m s^{-2}), q_v is the layer average water vapor mixing ratio between each model level (kg$_{\text{water}}$ kg$_{\text{air}}^{-1}$), dp is the depth between each model level over which q_v is computed (Pa), and V_n is the layer average horizontal wind (m s^{-1}) normal to a budget box edge over dp. Positive fluxes are assigned following the arrows in the map in Fig. 16. The southern and eastern cross sections are defined to match prevailing wind directions. Water vapor flux results are consistent with previous findings, both in terms of daily averages and hourly series. Highest values are found for M2P2 − ε and lowest values are found for M2P2 + ε. The SST0 line is closest to M2P2 + ε, while SST1, SST2, and SST3 lines lie between M2P2 and M2P2 − ε. It is noteworthy that the double-peaked water vapor flux evolution of all configurations except M2P2 − ε and M2P2 + ε is mainly a result of the nighttime contribution from segment BC and further daytime contribution from segment AB.

b. *The 27–29 December 2008 events*

Precipitation differences identified on 27 and 29 December 2008 (Fig. 7) are connected to each other; hence, the main features for these two days can be analyzed within the same general framework. The synoptic conditions for these days are characterized by an anticyclone centered over Scandinavia, affecting most of northwestern Europe. The Mediterranean Sea instead is dominated by low pressure: under these conditions, cold air masses pushed from the north by the anticyclone hit warmer air masses and can cause several consecutive weather fronts. In the second half of 26 December, two low-pressure systems, one coming from the western Mediterranean Sea and another one from northwestern Africa, merge near Malta, leading to a stationary low-pressure system centered off the coasts of Ionian Sea the following day. This system persists for one more day and then disappears in the early hours of 29 December.

Daily precipitation patterns simulated on 27 December (Fig. 17) show that precipitation differences caused by SST representation can be identified with events mainly affecting the eastern side of the region. It is important to remember that in these situations M2P2 is not the best configuration to match the observations. Table 7 shows that both 27 and 29 December are in fact nearly dry days;

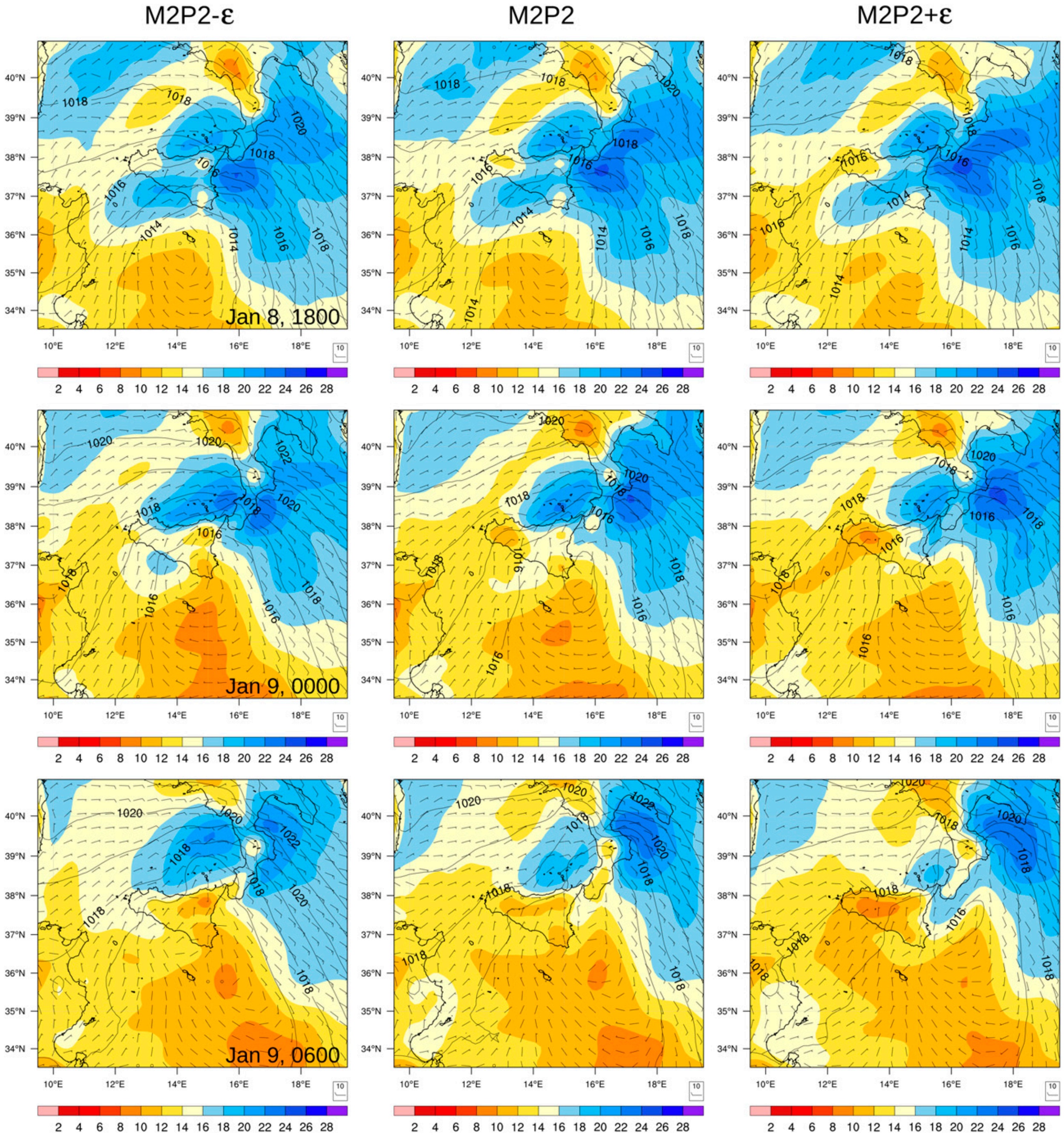

FIG. 11. Column IWV (kg m^{-2}) for configurations M2P2 − ε, M2P2, and M2P2 + ε at different times. The maps also show sea level pressure (contours; hPa) and 10-m winds (barbs; m s^{-1}).

hence, the quality of the different configurations with respect to matching observed data over land greatly depends on the distribution of simulated precipitation patterns over sea or land grid cells.

Although almost 1 K warmer on average, SST fields patterns and their relative differences (not shown) are similar to the previously discussed case of 9 January. Again, tracking sea level pressure minima helps to explain the spatial distribution of precipitation in the inner domain (Fig. 18). According to the synoptic conditions, the main track direction is southwest–northeast for all configurations. When more energy is released by SST boundary conditions (especially for M2P2 + ε and SST0), longer paths toward the

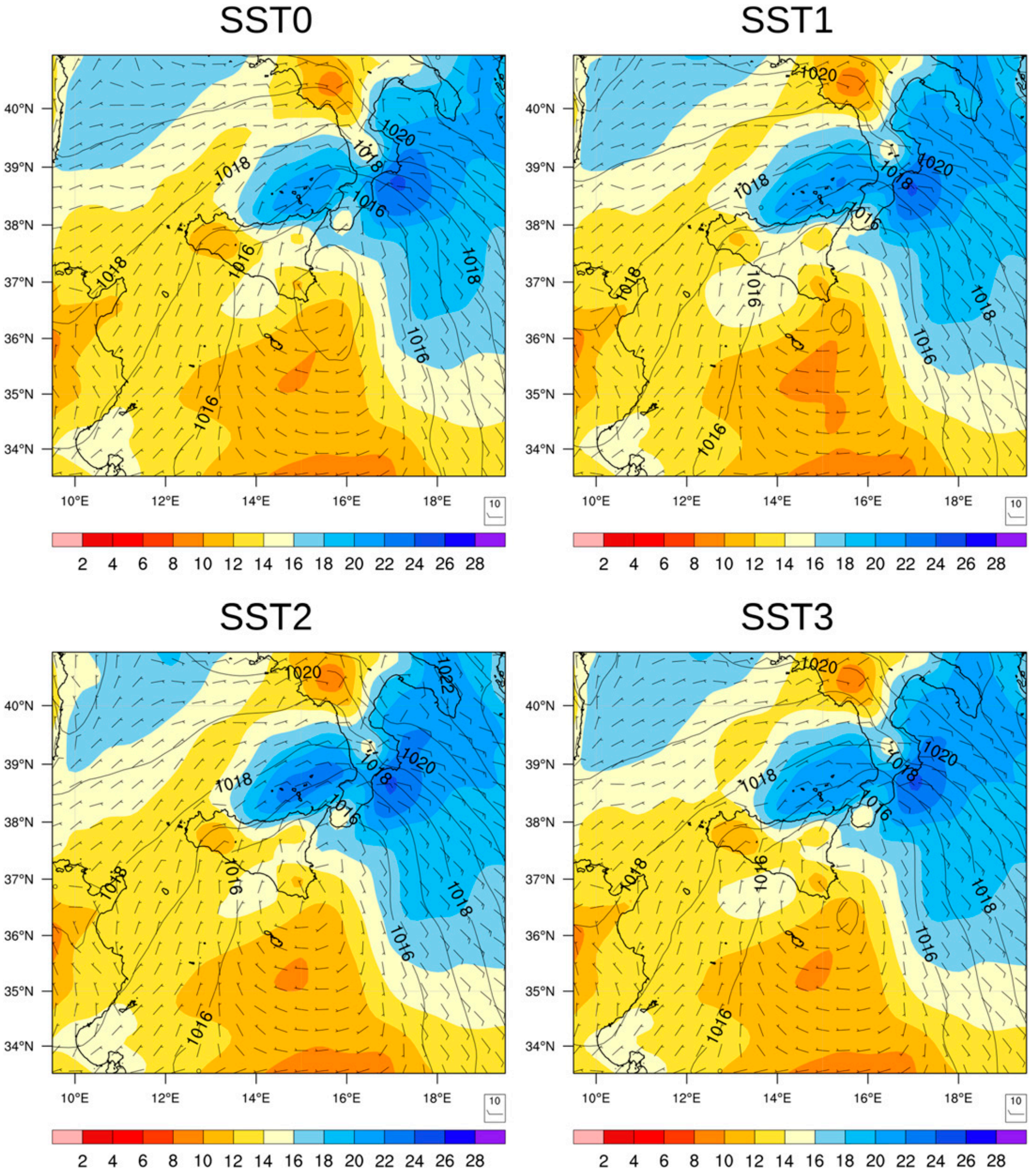

FIG. 12. As in Fig. 11, but for configurations SST0–SST3 at 0000 UTC 9 Jan.

northeast are possible and lower sea level pressure minima are reached (down to 1010 hPa for M2P2 + ε). Water vapor distributions can be related to pressure minima tracks through a simple rule, highlighted by the example given in Fig. 19, where differences between the configurations M2P2 − ε, M2P2, and M2P2 + ε are shown when moist air reaches the Calabrian Ionian coast: the warmer the SST, the more northern the contact point between moist air and land, and the higher but farther from the coast the IWV peaks. The IWV evolution can be explained more clearly in the inner domain. Tracks of IWV maxima (Fig. 20) from 2100 UTC 26 December to 1200 UTC 27 December confirm that the M2P2 + ε maxima are higher, but farther from the coast. The M2P2 − ε and M2P2 maxima, however, are not only closer to the coastline but also exhibit secondary maxima located farther north, which suggest that the whole coastline in between is dominated by a considerable amount of water vapor. This analysis perfectly agrees with the M2P2 − ε and M2P2 precipitation patterns in Fig. 17, where the same part of the coastline is subject to the highest rainfall. In Fig. 20, the tracks of IWV maxima for the SSTx configurations are omitted, since they are very close to each other

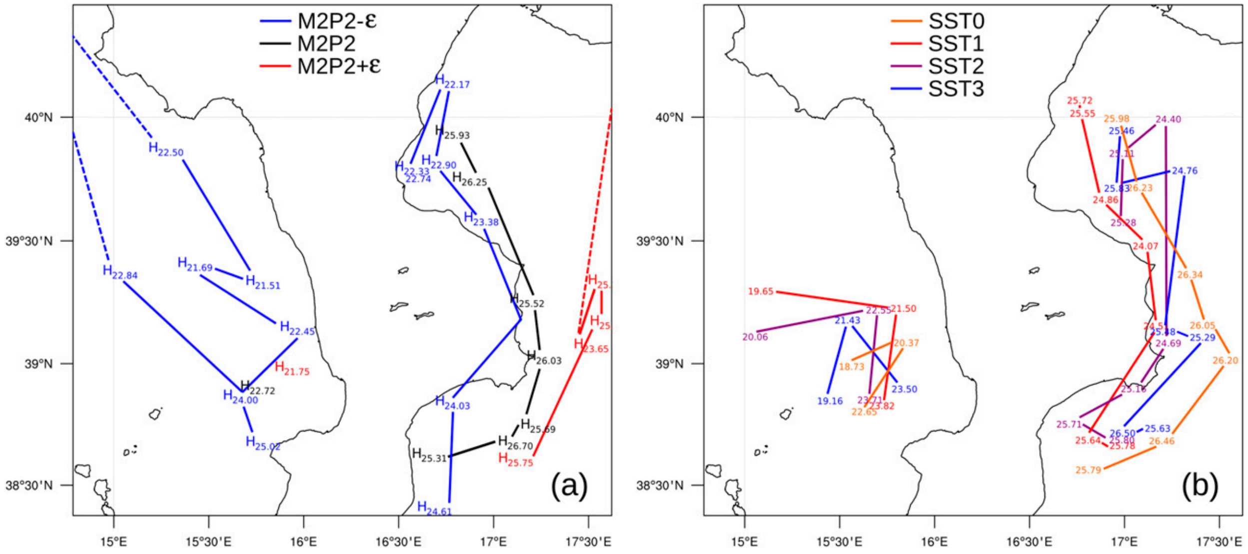

FIG. 13. Tracks of IWV maxima (kg m^{-2}) in the inner domain for different configurations. Values are shown for every 3 h from 0000 to 1800 UTC 9 Jan. Local minima exceeding a certain threshold (20.00 kg m^{-2} as a rule of thumb) in the Tyrrhenian Sea are also shown, starting at 0000 UTC 9 Jan.

and show several local maxima that would make the graph hard to read. However, we would like to note that absolute maxima of SST1, SST2, and SST3 are comparable to M2P2 − ε and M2P2.

The numerous similarities between the 27 December and 9 January situations point out that a specific class of events, namely, with a south–north or southwest–northeast direction and with tracks of pressure minima

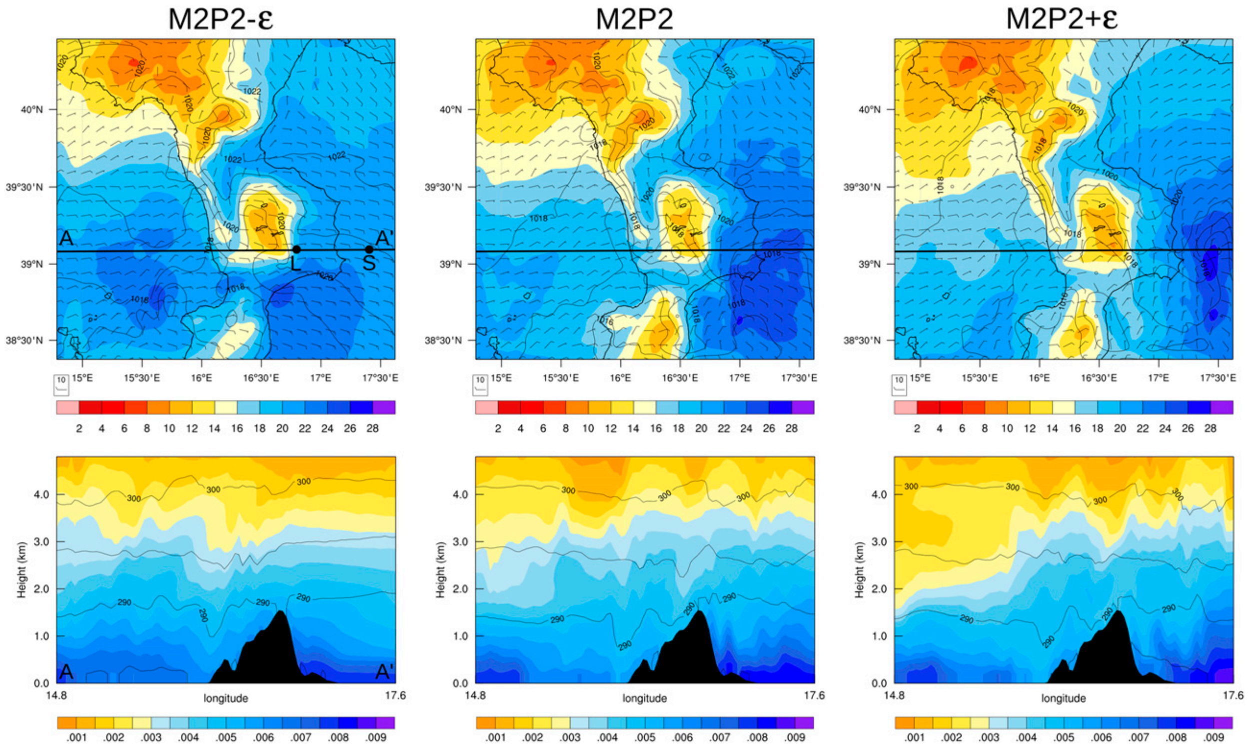

FIG. 14. (top) IWV (kg m^{-2}), sea level pressure (contours; hPa), and 10-m winds (barbs; m s^{-1}) for configurations M2P2 − ε, M2P2, and M2P2 + ε at 0200 UTC 9 Jan. (bottom) Corresponding cross sections along the segment AA′ of equivalent potential temperature (contours; K) and water vapor mixing ratio (color shaded; kg kg^{-1}).

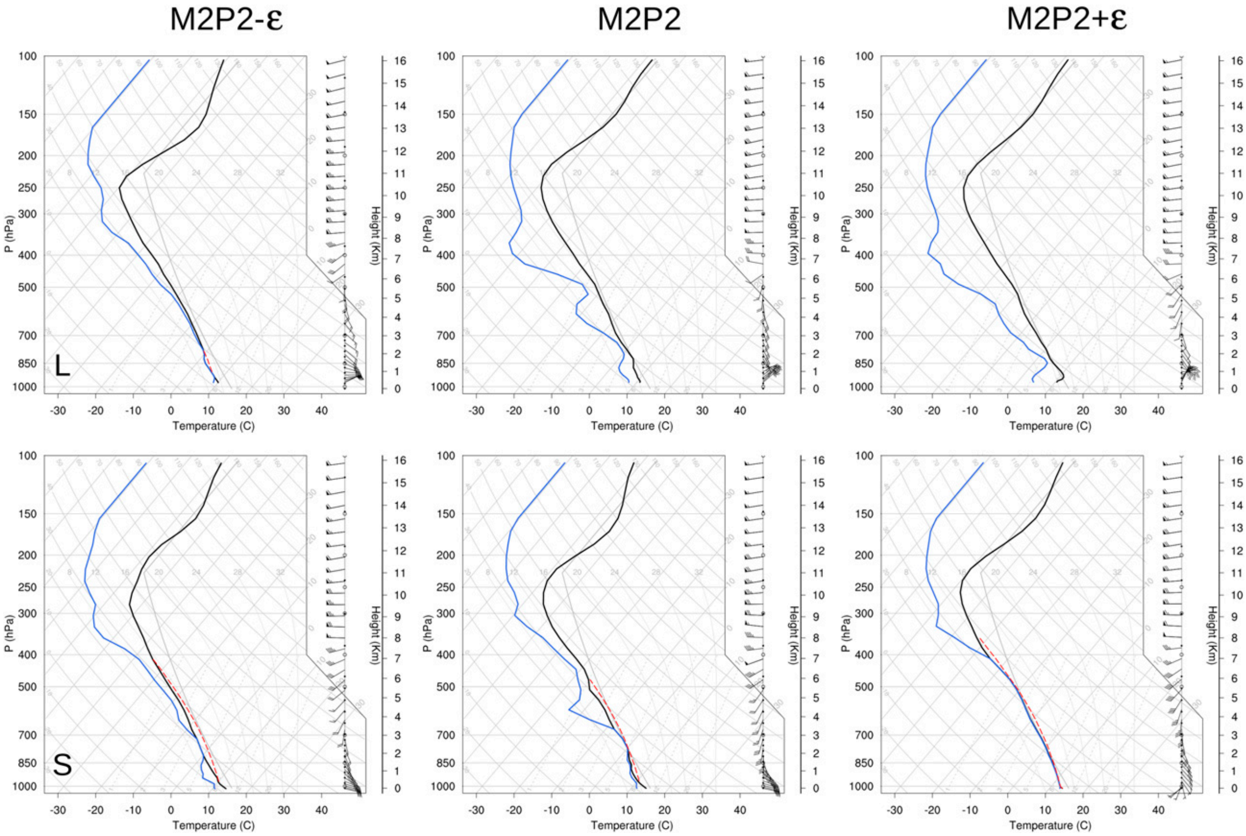

FIG. 15. Vertical profiles of temperature (black lines), dewpoint (blue lines), and parcel lapse rate (red dashed lines) for L and S points represented in Fig. 14, for configurations M2P2 − ε, M2P2, and M2P2 + ε at 0200 UTC 9 Jan. Also, wind speed and directions along the air columns (up to 16 km) are represented.

close enough to the coastline, is particularly affected by the coastal SST representation and/or a slight increase or decrease of SST values. The following analysis of 29 December is added for the sake of completion, although the synoptic condition is mainly determined by the initial conditions discussed above.

Most of the daily precipitation maps in Fig. 21 reveal two spatially separate clusters of simulated precipitation: one approximately at the center of the domain and the other one to the south. Where present, the southern precipitation features are related to a new event, developing in the second half of 29 December and

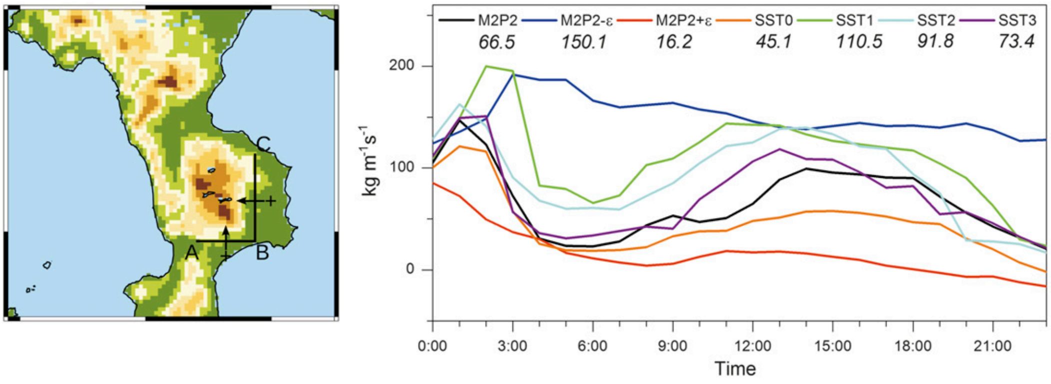

FIG. 16. Time series of hourly averaged water vapor flux (kg m^{-1} s^{-1}) on 9 Jan 2009, through section ABC. (left) Map with sign conventions; (right) daily average values.

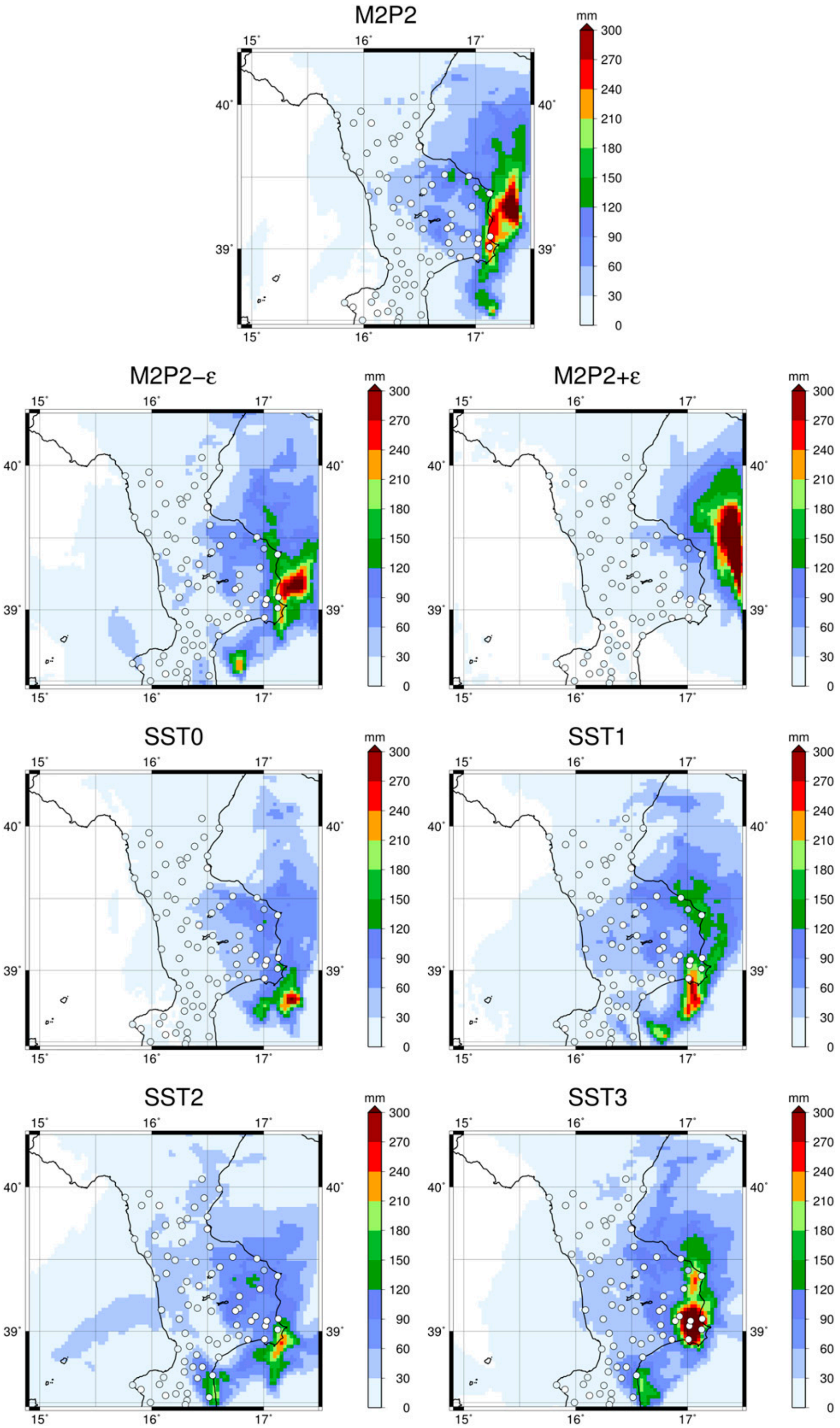

FIG. 17. Daily precipitation patterns in the inner domain on 27 Dec 2008, with observed data (colored circles; white circles represent null observed rain).

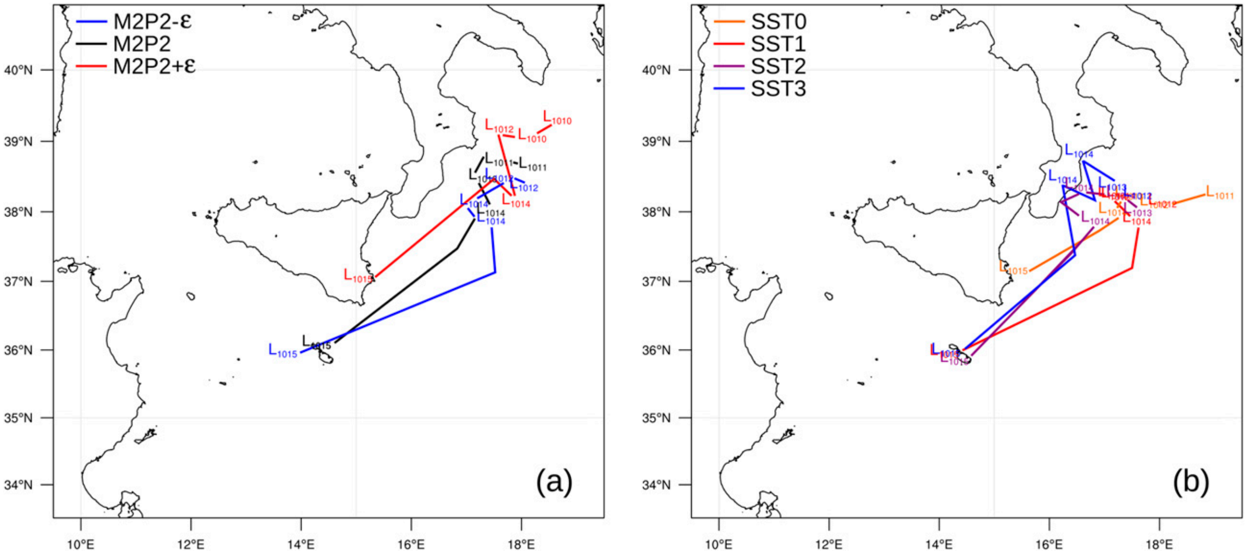

FIG. 18. Tracks of pressure minima for the different configurations extracted from the outer domain. Time steps considered are 2100 UTC 26 Dec and 0300, 0900, 1500, and 2100 UTC 27 Dec.

not considered in this analysis. Focusing on precipitation in the center of the domain, highest values (clearly induced by orographic effect) are provided by M2P2 − ε and M2P2. This behavior can be again explained by tracking the pressure minima for the different configurations (Fig. 22): tracks of pressure minima for both M2P2 − ε and M2P2 are directed toward the Calabrian topography. The SST*x* tracks, however, do not cross the Calabrian mountains: from 0300 to 0900 UTC 28 December, while M2P2 and M2P2 ± ε pressure minima move slightly northward, SST*x* pressure minima tend southward. These subtle differences, very difficult to explain, are sufficient for emphasizing distances between tracks and precipitation patterns. The configuration SST2, whose pressure minimum track is the farthest from the Calabrian coast, is the one providing the lowest precipitation rates on land.

4. Conclusions

A sensitivity analysis of modeled precipitation to SST representation in WRF long-term continuous simulations was performed for Calabria, a mountainous Mediterranean peninsula. In this region, spatial patterns and

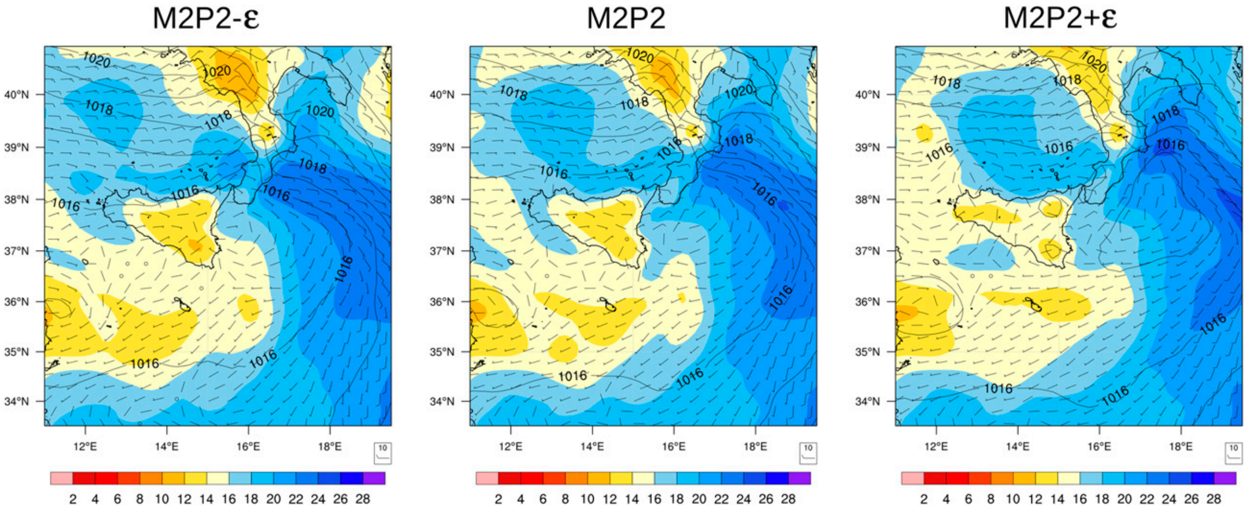

FIG. 19. Column IWV (kg m^{-2}) for configurations M2P2 − ε, M2P2, and M2P2 + ε at 0000 UTC 27 Dec. Maps also show sea level pressure (contours; hPa) and 10-m winds (barbs; m s^{-1}).

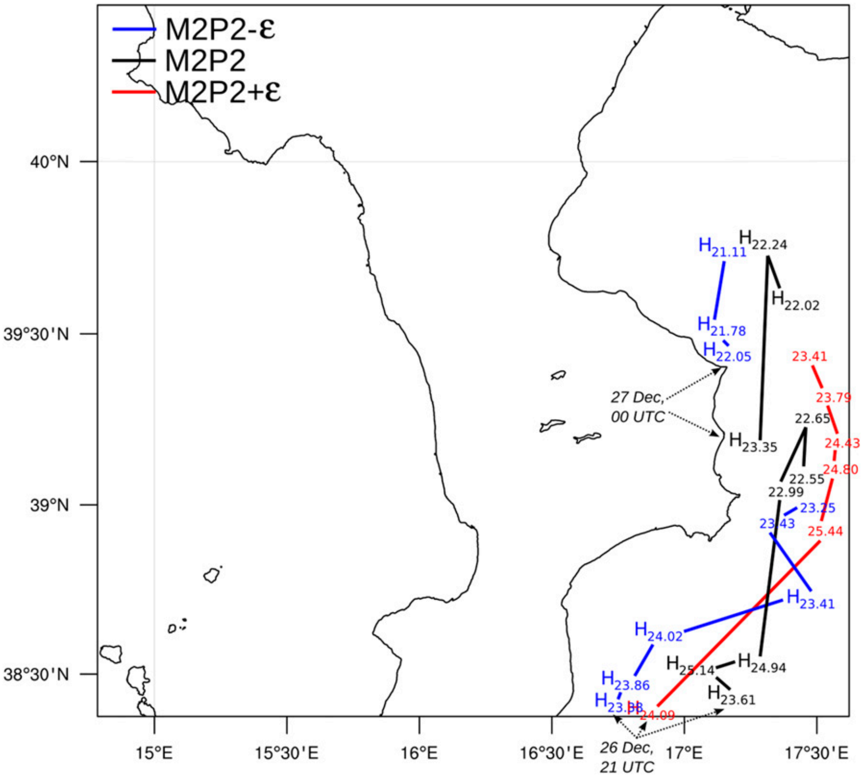

FIG. 20. Tracks of IWV maxima (kg m^{-2}) in the inner domain for configurations M2P2 − ε, M2P2, and M2P2 + ε. Values are shown for every 3 h from 2100 UTC 26 Dec to 1200 UTC 27 Dec. From 0000 to 0600 UTC 27 Dec, further relevant local minima are shown for M2P2 − ε and M2P2.

intensities of rain events are strongly related to the combined effects of complex orography and the surrounding sea. Prior to this study, a detailed investigation of long-term simulations has not been undertaken for this region. Therefore, a parameterization analysis was first carried out, focusing on a number of parameterization schemes and evaluated for both wet and dry periods of several months. The SST representation in this analysis was specifically managed, ingesting gridded data directly from NOAA OISST2 and NCEP RTG SST (which are also used by ERA-Interim) into the WRF lower boundary conditions file. The optimal model configuration M2P2 showed an average bias of −5.4 mm with respect to observed accumulated values over the 3-month-long wet period (average observed value equal to 743.5 mm) and an average bias of +26.3 mm for the 12-month-long dry period (average observed value equal to 832.7 mm). It thus represented well the accumulated spatial precipitation patterns in both periods as well as the main features on a daily scale.

The study of the sensitivity of M2P2 precipitation patterns to SST representation was carried out by defining new configurations SST0, SST1, SST2, and SST3 (where SST fields are derived from the ERA-Interim dataset using different interpolation schemes within the WPS) plus M2P2 ± ε configurations for the 3-month-long wet period. This study allowed for several conclusions.

1) From the perspective of long-term simulations, the effects of SST representation on accumulated precipitation were generally small. More precisely, for the Calabrian land grid cells, an overall deviation of −0.6%, −1.4%, and −1.9% for SST1, SST2, and SST3, respectively, was found compared to M2P2. Similarly, a bias of +2.4% and −1.5% was derived for M2P2 − ε and M2P2 + ε. The extremely simple management of near-coastline SST by SST0 led to a bias of −9.0%.
2) From the perspective of individual events, however, three specific cases with important differences were detected. These events were identified based on daily precipitation differences. Further analyses showed that main differences in precipitation patterns were caused by specific synoptic situations, connected to pressure systems moving from the African coast to

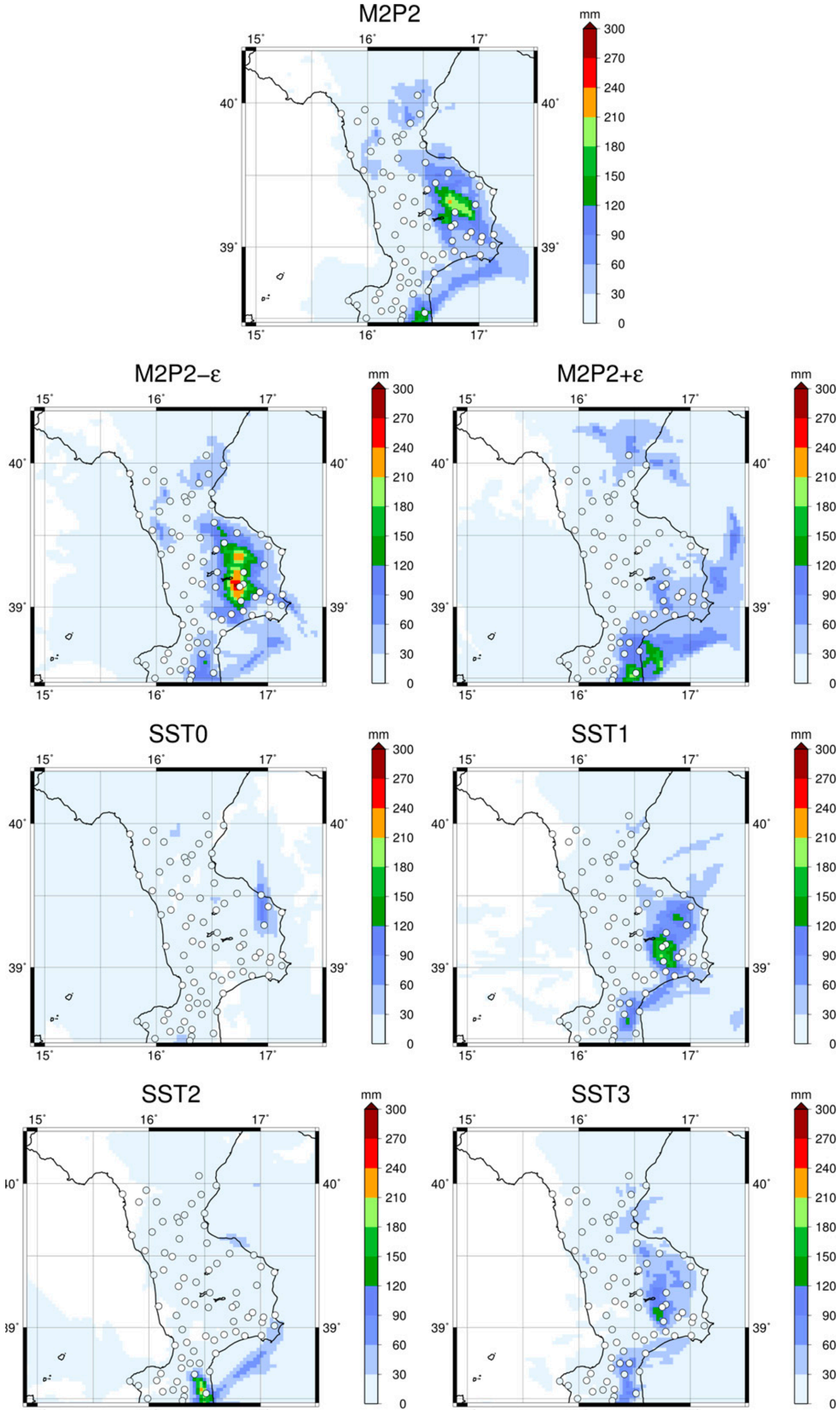

FIG. 21. Daily precipitation patterns in the inner domain on 29 Dec 2008, with observed data (circles).

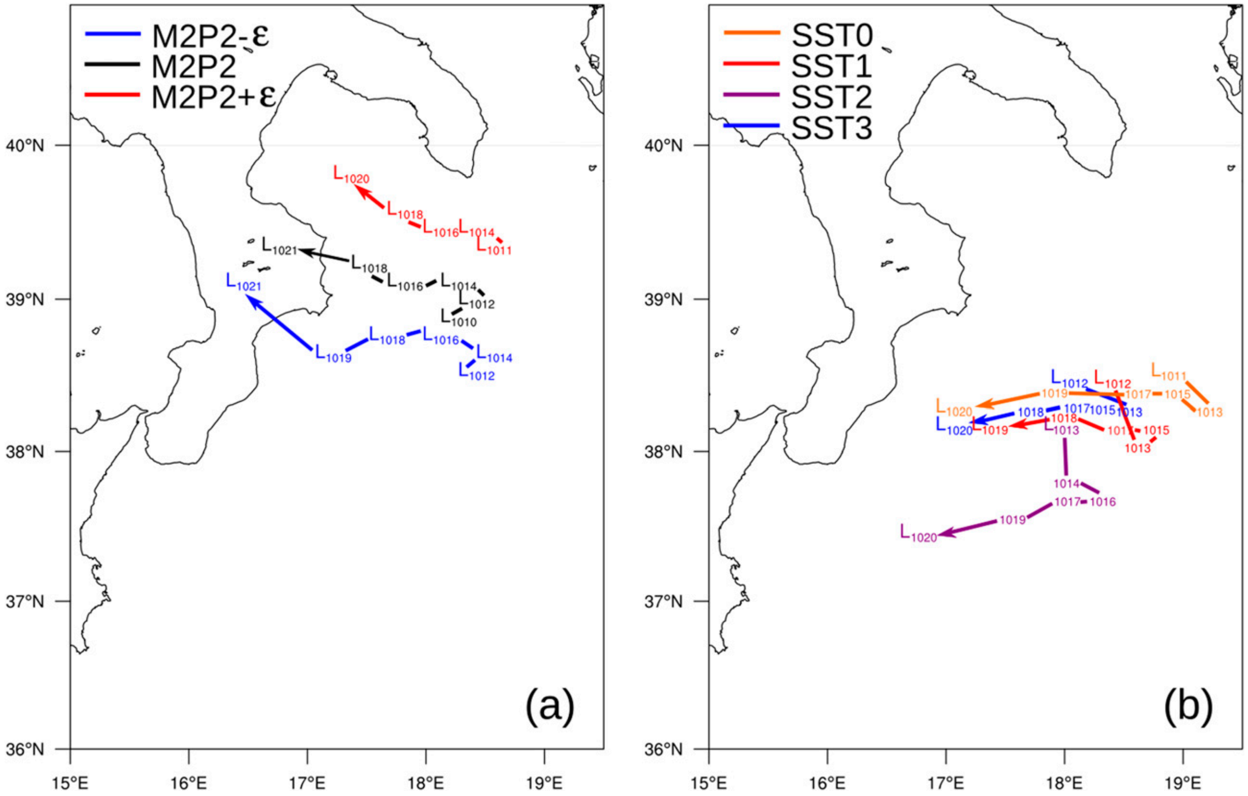

FIG. 22. Tracks of pressure minima for the different configurations extracted from the outer domain. Time steps considered are 0300, 0900, 1500, and 2100 UTC 28 Dec and 0300 and 0900 UTC 29 Dec.

the north and approaching the Sicilian and Calabrian coastlines. These kinds of events can lead to significant precipitation patterns either over eastern Calabria coastal land areas (e.g., 9 January event) or over sea (e.g., 27–29 December event). Slight shifts in paths of the weather fronts, caused by minor variations of SST values, led to major changes in modeled precipitation, depending on the capability of the wet air masses to reach the mountain ranges close to the coast, where the rainfall intensity is enhanced by orographic effects. The analysis performed here showed that in these situations the SST representation plays a major role.

3) Interpolation methods mainly affect near-coastline SST values. As was shown for both the SST0 and the SST2 configurations, it is not advisable to use only complex interpolation methods when the domain includes complex coastlines. Further, the SST2 configuration dramatically underestimated SST values (even down to SST < 273.15 K) because of colder winter LSTs. Conversely, relying on simpler methods like 16-point or 4-point average interpolation only (SST1 configuration) led to SST representations closer to the direct ingestion of NCEP RTG SST to grids. However, SST average values in configurations SST1 and SST3 also showed biases of about -0.3 and -0.4 K with respect to M2P2, due to the smoothing techniques adopted by the interpolation methods. It is noteworthy that, in turn, on 9 January 2009 the M2P2 SST field was on average 0.3 K lower than high-resolution satellite observations.

4) A perfect representation of SST does not imply by default a better performance of a specific configuration compared with others. Despite the good performance of M2P2 for the 9 January event, the case study of 27–29 December suggested that factors other than a correct representation of SST can have more influence on the accuracy of the model. Nevertheless, when trying to identify reasons for weak performances of numerical weather models like WRF in coastal areas, an accurate description of SST can help to narrow down the search.

Acknowledgments. This work was cofinanced by the program ‘‘Borse Post-doc all’estero UniCal,’’ POR Calabria–European Social Fund 2007/2013, Axis 4 ‘‘Capitale umano,’’ Operative objective M.2. The authors gratefully acknowledge Dr. M. M. Miglietta for providing information on the physical parameterization used in WRF operational forecasts at ISAC-CNR, Lecce. The Centro Funzionale Multirischi–ARPACAL (Calabria Region) is also acknowledged for providing daily rainfall data. The authors thank Editor Joe Turk and the anonymous reviewers for their critical and constructive reviews, which helped to improve the quality of this paper. Finally, the authors thank Richard Foreman and Dominikus Heinzeller from the Karlsruhe Institute of Technology (KIT) for their valuable suggestions to improve the quality of the manuscript.

REFERENCES

Bertotti, L., M. M. Miglietta, and S. Davolio, 2009: Coupling of high-resolution meteorological and wave models over southern Italy. *Nat. Hazards Earth Syst. Sci.,* **9,** 1267–1275, doi:10.5194/nhess-9-1267-2009.

Boé, J., A. Hall, F. Colas, J. C. McWilliams, X. Qu, J. Kurian, and S. B. Kapnick, 2011: What shapes mesoscale wind anomalies in coastal upwelling zones? *Climate Dyn.,* **36,** 2037–2049, doi:10.1007/s00382-011-1058-5.

Bond, N. A., M. F. Cronin, and M. Garvert, 2010: Atmospheric sensitivity to SST near the Kuroshio Extension during the extratropical transition of Typhoon Tokage. *Mon. Wea. Rev.,* **138,** 2644–2663, doi:10.1175/2010MWR3198.1.

Bongirwar, V., V. Rakesh, C. M. Kishtawal, and P. C. Joshi, 2011: Impact of satellite observed microwave SST on the simulation of tropical cyclones. *Nat. Hazards,* **58,** 929–944, doi:10.1007/s11069-010-9699-y.

Booth, J. F., L. Thompson, J. Patoux, and K. A. Kelly, 2012: Sensitivity of midlatitude storm intensification to perturbations in the sea surface temperature near the Gulf Stream. *Mon. Wea. Rev.,* **140,** 1241–1256, doi:10.1175/MWR-D-11-00195.1.

Borge, R., V. Alexandrov, J. J. del Vas, J. Lumbreras, and E. Rodrguez, 2008: A comprehensive sensitivity analysis of the WRF Model for air quality applications over the Iberian Peninsula. *Atmos. Environ.,* **42,** 8560–8574, doi:10.1016/j.atmosenv.2008.08.032.

Caldwell, P., H.-N. S. Chin, D. C. Bader, and G. Bala, 2009: Evaluation of a WRF dynamical downscaling simulation over California. *Climatic Change,* **95,** 499–521, doi:10.1007/s10584-009-9583-5.

Case, J. L., S. V. Kumar, J. Srikishen, and G. J. Jedlovec, 2011: Improving numerical weather predictions of summertime precipitation over the southeastern United States through a high-resolution initialization of the surface state. *Wea. Forecasting,* **26,** 785–807, doi:10.1175/2011WAF2222455.1.

Cha, Y. M., H. W. Lee, and S. H. Lee, 2011: Impacts of the high-resolution sea surface temperature distribution on modeled snowfall formation over the Yellow Sea during a cold-air outbreak. *Wea. Forecasting,* **26,** 487–503, doi:10.1175/WAF-D-10-05019.1.

Chen, F., S. Miao, M. Tewari, J.-W. Bao, and H. Kusaka, 2011: A numerical study of interactions between surface forcing and sea breeze circulations and their effects on stagnation in the greater Houston area. *J. Geophys. Res.,* **116,** D12105, doi:10.1029/2010JD015533.

Chen, S. H., and W. Y. Sun, 2002: A one-dimensional time dependent cloud model. *J. Meteor. Soc. Japan,* **80,** 99–118, doi:10.2151/jmsj.80.99.

Dee, D. P., and Coauthors, 2011: The ERA-Interim reanalysis: Configuration and performance of the data assimilation system. *Quart. J. Roy. Meteor. Soc.,* **137,** 553–597, doi:10.1002/qj.828.

Dudhia, J., 1989: Numerical study of convection observed during the winter monsoon experiment using a mesoscale two-dimensional model. *J. Atmos. Sci.,* **46,** 3077–3107, doi:10.1175/1520-0469(1989)046<3077:NSOCOD>2.0.CO;2.

——, S. Y. Hong, and K. S. Lim, 2008: A new method for representing mixed-phase particle fall speeds in bulk microphysics parameterizations. *J. Meteor. Soc. Japan,* **86A,** 33–44, doi:10.2151/jmsj.86A.33.

Flaounas, E., S. Janicot, S. Bastin, and R. Roca, 2012: The West African monsoon onset in 2006: Sensitivity to surface albedo, orography, SST and synoptic scale dry-air intrusions using WRF. *Climate Dyn.,* **38,** 685–708, doi:10.1007/s00382-011-1255-2.

Flesch, T. K., and G. W. Reuter, 2012: WRF Model simulation of two Alberta flooding events and the impact of topography. *J. Hydrometeor.,* **13,** 695–708, doi:10.1175/JHM-D-11-035.1.

Givati, A., B. Lynn, Y. Liu, and A. Rimmer, 2012: Using the WRF Model in an operational streamflow forecast system for the Jordan River. *J. Appl. Meteor. Climatol.,* **51,** 285–299, doi:10.1175/JAMC-D-11-082.1.

Grell, G. A., and D. Dévényi, 2002: A generalized approach to parameterizing convection combining ensemble and data assimilation techniques. *Geophys. Res. Lett.,* **29,** 1693, doi:10.1029/2002GL015311.

Hong, S. Y., and J. W. Lee, 2009: Assessment of the WRF Model in reproducing a flash-flood heavy rainfall event over Korea. *Atmos. Res.,* **93,** 818–831, doi:10.1016/j.atmosres.2009.03.015.

——, J. Dudhia, and S. H. Chen, 2004: A revised approach to ice microphysical processes for the bulk parameterization of clouds and precipitation. *Mon. Wea. Rev.,* **132,** 103–120, doi:10.1175/1520-0493(2004)132<0103:ARATIM>2.0.CO;2.

——, Y. Noh, and J. Dudhia, 2006: A new vertical diffusion package with an explicit treatment of entrainment processes. *Mon. Wea. Rev.,* **134,** 2318–2341, doi:10.1175/MWR3199.1.

Janjić, Z. I., 2002: Nonsingular implementation of the Mellor–Yamada level 2.5 scheme in the NCEP meso model. NCEP Office Note 437, 61 pp. [Available online at www.emc.ncep.noaa.gov/officenotes/newernotes/on437.pdf.]

Jolliff, J. K., J. C. Kindle, I. Shulman, B. Penta, M. A. M. Friedrichs, R. Helber, and R. A. Arnone, 2009: Summary diagrams for coupled hydrodynamic–ecosystem model skill assessment. *J. Mar. Syst.,* **76,** 64–82, doi:10.1016/j.jmarsys.2008.05.014.

Jung, S.-H., E.-S. Im, and S.-O. Han, 2012: The effect of topography and sea surface temperature on heavy snowfall in the Yeongdong region: A case study with high resolution WRF simulation. *Asia-Pac. J. Atmos. Sci.,* **48,** 259–273, doi:10.1007/s13143-012-0026-2.

Kain, J. S., 2004: The Kain–Fritsch convective parameterization: An update. *J. Appl. Meteor.,* **43,** 170–181, doi:10.1175/1520-0450(2004)043<0170:TKCPAU>2.0.CO;2.

LaCasse, K. M., M. E. Splitt, S. M. Lazarus, and W. M. Lapenta, 2008: The impact of high-resolution sea surface temperatures on the simulated nocturnal Florida marine boundary layer. *Mon. Wea. Rev.,* **136,** 1349–1372, doi:10.1175/2007MWR2167.1.

Lebeaupin Brossier, C., and P. Drobinski, 2009: Numerical high-resolution air–sea coupling over the Gulf of Lions during two tramontane/mistral events. *J. Geophys. Res.,* **114,** D10110, doi:10.1029/2008JD011601.

Lin, Y. L., R. D. Farley, and H. D. Orville, 1983: Bulk parameterization of the snow field in a cloud model. *J. Climate Appl. Meteor.,* **22,** 1065–1092, doi:10.1175/1520-0450(1983)022<1065:BPOTSF>2.0.CO;2.

Mastrangelo, D., K. Horvat, A. Riccio, and M. M. Miglietta, 2011: Mechanisms for convection development in a long-lasting heavy precipitation event over southeastern Italy. *Atmos. Res.,* **100,** 586–602, doi:10.1016/j.atmosres.2010.10.010.

Mendicino, G., A. Senatore, and P. Versace, 2008: A groundwater resource index (GRI) for drought monitoring and forecasting in a Mediterranean climate. *J. Hydrol.,* **357,** 282–302, doi:10.1016/j.jhydrol.2008.05.005.

Miglietta, M. M., and A. Regano, 2008: An observational and numerical study of a flash-flood event over south-eastern Italy. *Nat. Hazards Earth Syst. Sci.,* **8,** 1417–1430, doi:10.5194/nhess-8-1417-2008.

——, A. Moscatello, D. Conte, G. Mannarini, G. Lacorata, and R. Rotunno, 2011: Numerical analysis of a Mediterranean hurricane over south-eastern Italy: Sensitivity experiments to sea surface temperature. *Atmos. Res.,* **101,** 412–426, doi:10.1016/j.atmosres.2011.04.006.

Mlawer, E. J., S. J. Taubman, P. D. Brown, M. J. Iacono, and S. A. Clough, 1997: Radiative transfer for inhomogeneous atmosphere: RRTM, a validated correlated-*k* model for the longwave. *J. Geophys. Res.,* **102,** 16 663–16 682, doi:10.1029/97JD00237.

Muller, H., F. Dumas, B. Blanke, and V. Mariette, 2007: High-resolution atmospheric forcing for regional oceanic model: The Iroise Sea. *Ocean Dyn.,* **57,** 375–400, doi:10.1007/s10236-007-0115-4.

Nash, J. E., and J. V. Sutcliffe, 1970: River flow forecasting through conceptual models part I—A discussion of principles. *J. Hydrol.,* **10,** 282–290, doi:10.1016/0022-1694(70)90255-6.

Neiman, P. J., F. M. Ralph, B. J. Moore, M. Hughes, K. M. Mahoney, J. M. Cordeira, and M. D. Dettinger, 2013: The landfall and inland penetration of a flood-producing atmospheric river in Arizona. Part I: Observed synoptic-scale, orographic, and hydrometeorological characteristics. *J. Hydrometeor.,* **14,** 460–484, doi:10.1175/JHM-D-12-0101.1.

Papanastasiou, D. K., D. Melas, and I. Lissaridis, 2010: Study of wind field under sea breeze conditions; An application of WRF Model. *Atmos. Res.,* **98,** 102–117, doi:10.1016/j.atmosres.2010.06.005.

Ratnam, J. V., S. K. Behera, Y. Masumoto, K. Takahashi, and T. Yamagata, 2012: A simple regional coupled model experiment for summer-time climate simulation over southern Africa. *Climate Dyn.,* **39,** 2207–2217, doi:10.1007/s00382-011-1190-2.

Rebora, N., and Coauthors, 2013: Extreme rainfall in the Mediterranean: What can we learn from observations? *J. Hydrometeor.,* **14,** 906–922, doi:10.1175/JHM-D-12-083.1.

Rutledge, S. A., and P. V. Hobbs, 1984: The mesoscale and microscale structure and organization of clouds and precipitation in midlatitude cyclones. XII: A diagnostic modeling study of precipitation development in narrow cloud-frontal rainbands. *J. Atmos. Sci.,* **41,** 2949–2972, doi:10.1175/1520-0469(1984)041<2949:TMAMSA>2.0.CO;2.

Schurmann, G. J., A. Algieri, I. M. Hedgecock, G. Manna, N. Pirrone, and F. Sprovieri, 2009: Modelling local and synoptic scale influences on ozone concentrations in a topographically complex region of southern Italy. *Atmos. Environ.,* **43,** 4424–4434, doi:10.1016/j.atmosenv.2009.06.017.

Senatore, A., G. Mendicino, G. Smiatek, and H. Kunstmann, 2011: Regional climate change projections and hydrological impact analysis for a Mediterranean basin in southern Italy. *J. Hydrol.,* **399,** 70–92, doi:10.1016/j.jhydrol.2010.12.035.

Sijikumar, S., and K. Rajeev, 2012: Role of the Arabian Sea warm pool on the precipitation characteristics during the monsoon onset period. *J. Climate,* **25,** 1890–1899, doi:10.1175/JCLI-D-11-00286.1.

Skamarock, W. C., and Coauthors, 2008: A description of the Advanced Research WRF version 3. NCAR Tech. Note NCAR/TN-475+STR, 113 pp., doi:10.5065/D68S4MVH.

Smith, B. L., S. E. Yuter, P. J. Neiman, and D. E. Kingsmill, 2010: Water vapor fluxes and orographic precipitation over Northern California associated with a landfalling atmospheric river. *Mon. Wea. Rev.,* **138,** 74–100, doi:10.1175/2009MWR2939.1.

Song, Q., D. Chelton, S. Esbensen, N. Thum, and L. O'Neill, 2009: Coupling between sea surface temperature and low-level winds in mesoscale numerical models. *J. Climate,* **22,** 146–164, doi:10.1175/2008JCLI2488.1.

Stensrud, D. J., 2007: *Parameterization Schemes: Keys to Understanding Numerical Weather Prediction Models.* Cambridge University Press, 488 pp.

Taylor, K. E., 2001: Summarizing multiple aspects of model performance in a single diagram. *J. Geol. Res.,* **106,** 7183–7192, doi:10.1029/2000JD900719.

Thompson, G., P. R. Field, R. M. Rasmussen, and W. D. Hall, 2008: Explicit forecasts of winter precipitation using an improved bulk microphysics scheme. Part II: Implementation of a new snow parameterization. *Mon. Wea. Rev.,* **136,** 5095–5115, doi:10.1175/2008MWR2387.1.

van Dijke, D., and B. Vonk, 2011: Skin surface temperature interpolation improvement. *Extended Abstracts, 12th Annual WRF Users Workshop,* Boulder, CO, NCAR, 3 pp. [Available online at http://www2.mmm.ucar.edu/wrf/users/workshops/WS2011/Extended%20Abstracts%202011/P5_VanDijke_ExtendedAbstract_11.pdf.]

Zeng, X., and A. Beljaars, 2005: A prognostic scheme of sea surface skin temperature for modeling and data assimilation. *Geophys. Res. Lett.,* **32,** L14605, doi:10.1029/2005GL023030.